crystals

MDPI

Article

The Effect of Sintering Atmosphere and Temperature on Densification, Grain Growth Behavior and Electrical Properties of $0.685(Na_{0.5}Bi_{0.5})TiO_3$-$0.065BaTiO_3$-$0.25SrTiO_3$ Ceramics

Nazım Ecebaş [1], Tran Thi Huyen Tran [1], John G. Fisher [1,*], Jong-Sook Lee [1,*], Woo-Jin Choi [2], Yeon-Bee Han [2] and Wook Jo [2]

[1] Department of Materials Science and Engineering, Chonnam National University, 77 Yongbong-ro, Buk-gu, Gwangju 61186, Republic of Korea
[2] School of Materials Science and Engineering, Ulsan National Institute of Science and Technology, 50 UNIST-gil, Eonyang-Eup, Ulju-gun, Ulsan 44919, Republic of Korea
* Correspondence: johnfisher@jnu.ac.kr (J.G.F.); jongsook@jnu.ac.kr (J.-S.L.)

Abstract

$(Na_{0.5}Bi_{0.5})TiO_3$-$BaTiO_3$-$SrTiO_3$-based lead-free piezoelectric ceramics are one of the possible replacements for $Pb(Zr_{1-x}Ti_x)O_3$. Although they are considered a promising alternative actuator material due to their large electric-field-induced strains, they have several drawbacks, such as large strain hysteresis and the requirement of a high electric field to obtain large electric-field-induced strains. Sintering parameters strongly influence the electrical properties. Thus, the effect of sintering parameters, including atmosphere (air/oxygen), temperature (1150 °C~1250 °C) and holding time (1~20 h) on the sintering behavior of $0.685(Na_{0.5}Bi_{0.5})TiO_3$-$0.065BaTiO_3$-$0.25SrTiO_3$ electroceramics was studied. Then, the influence of sintering atmosphere on the piezoelectric, ferroelectric and dielectric properties of $0.685(Na_{0.5}Bi_{0.5})TiO_3$-$0.065BaTiO_3$-$0.25SrTiO_3$ electroceramics sintered at 1250 °C for 1 h was investigated. Sintering in oxygen improves density and restrains grain growth including abnormal grain growth. $0.685(Na_{0.5}Bi_{0.5})TiO_3$-$0.065BaTiO_3$-$0.25SrTiO_3$ electroceramics sintered in oxygen exhibit smaller grain size, higher density, similar inverse piezoelectric coefficient d_{33}^* and lower strain hysteresis compared to air-sintered samples. The effect of sintering atmosphere on grain growth is explained using the mixed control mechanism of boundary migration.

Keywords: $(Na_{0.5}Bi_{0.5})TiO_3$; lead-free piezoelectric; sintering; grain growth; dielectric properties; ferroelectric properties; piezoelectric properties

Academic Editors: Nengneng Luo, Junjun Wang, Xudong Qi, Linjing Liu, Jie Wu and Kai Li

Received: 17 January 2026
Revised: 1 February 2026
Accepted: 5 February 2026
Published: 16 February 2026

1. Introduction

Ferroelectric and piezoelectric materials play a critical role in various electronic devices and microelectromechanical systems, because of their outstanding electromechanical response [1–6]. Lead zirconate titanate, $Pb(Zr_{1-x}Ti_x)O_3$ (PZT), has become the dominant material for many piezoelectric applications such as transducers, sensors and actuators because of its good properties [7,8]. This situation leads to increasing environmental concerns because PZT contains more than 60 wt % lead [9]. Environmental legislation in the European Union, the US and some parts of Asia have limited the usage of Pb because of its toxicity [10–13]. Such legislation has encouraged the development of new lead-free materials to replace PZT [9,14,15]. Due to its large electric-field-induced strains, $(Na_{0.5}Bi_{0.5})TiO_3$

https://doi.org/10.3390/cryst16020143

(NBT)-based materials are promising candidates to replace lead containing piezoelectric ceramics for actuator applications [11,16–20].

Practical applications for NBT are limited by some difficulties such as high dielectric loss, leakage current and coercive field, low electrical breakdown strength and negative electric-field-induced strains [13,16,20–28]. To enhance the electrical properties, NBT-based solid solutions, e.g., $(Na_{0.5}Bi_{0.5})TiO_3$-$NaNbO_3$ [29,30], $(Na_{0.5}Bi_{0.5})TiO_3$-$BaTiO_3$ [13,23,31], $(Na_{0.5}Bi_{0.5})TiO_3$-$(K_{0.5}Bi_{0.5})TiO_3$ [32,33], and $(Na_{0.5}Bi_{0.5})TiO_3$-$SrTiO_3$ [34,35] have been studied. Compositions close to a morphotropic phase boundary (MPB) have lower coercive field and improved piezoelectric properties [14,23,31].

NBT shows relaxor behavior [36]. Relaxor materials can be divided into two types, non-ergodic and ergodic [16,37]. Under a strong enough electric field, a non-ergodic relaxor can permanently transform into a ferroelectric state while an ergodic relaxor undergoes a reversible transformation into a ferroelectric state. Above the ferroelectric–relaxor transition temperature (T_{FR}), the ferroelectric state in non-ergodic relaxors is disturbed and transforms back to the relaxor state [38,39]. Pure NBT also has a depolarization temperature (T_d) at ~185 °C [27,30,40,41]. At this temperature, the ferroelectric and direct piezoelectric properties are degraded [42,43]. A transition from the long-range ferroelectric to the relaxor phase was reported at temperatures around T_d [44].

At temperatures around T_d, NBT undergoes an electric-field-induced transition between the relaxor and ferroelectric phases which is accompanied by a large strain. This transition is reversible upon removal of the electric field, with low or zero remanent strain, which is the cause of the large electric-field-induced strains [16,20,27]. Such large electric-field-induced strains (e.g., 0.45% under an electric field of 8 kV/mm) can also exist at room temperature when T_{FR} or T_d is shifted to room temperature by chemical modification [17,18,45]. The cause of these large strains has been suggested to be an antiferroelectric-ferroelectric phase transition [17], 90°-domain switching in the tetragonal phase [46] or a reversible phase transition of an ergodic relaxor to a ferroelectric phase [16]. A large number of NBT-based solid solutions with giant electric-field-induced strains at room temperature have been developed such as $(Na_{0.5}Bi_{0.5})TiO_3$-$NaNbO_3$ [30], $(Na_{0.5}Bi_{0.5})TiO_3$-$SrTiO_3$ [34,47], $(Na_{0.5}Bi_{0.5})TiO_3$-$KNbO_3$ [30] and $(Na_{0.5}Bi_{0.5})TiO_3$-$BaZrO_3$ [48]. Nevertheless, there are three essential drawbacks in these systems [49]. First, a large electric field of more than 6 kV/mm is often needed to induce the relaxor to ferroelectric phase transition and achieve large strain [49–52]. Secondly, the strain usually occurs with large hysteresis ($\eta = \Delta S/S_{max}$, where ΔS is the difference in strain at ½ E_{max} as the electric field increases and decreases) [11]. The large electric field limits their practical application as actuators while the large hysteresis decreases actuation precision and generates more heat [11,16]. Lastly, the change in achievable electrostrain with temperature limits the working temperature range for actuators [49].

$SrTiO_3$ is a paraelectric material with a room temperature undistorted cubic perovskite structure [53]. Enhancement of the piezoelectric properties of NBT-based materials with addition of $SrTiO_3$ has been reported [34,47,54,55]. For example, Hiruma et al. observed a strain of 0.29% and d_{33}* of 488 pm/V in $0.72(Na_{0.5}Bi_{0.5})TiO_3$-$0.28SrTiO_3$ [34]. Wang et al. reported that $SrTiO_3$ addition to $0.8(Na_{0.5}Bi_{0.5})TiO_3$-$0.2(Bi_{0.5}K_{0.5})TiO_3$ results in the disruption of ferroelectric order, resulting in a non-polar phase at zero electric field and a reversible electric-field-induced phase transition [54]. Addition of $SrTiO_3$ is also effective in reducing the electric field required to generate high strains in NBT and NBT-based materials [56,57]. Wang et al. reported that large electric-field-induced strains at moderate electric fields of 4 kV/mm occur with the addition of $SrTiO_3$ to $(Na_{0.5}Bi_{0.5})TiO_3$-$BaTiO_3$ ceramics [58,59].

Oxide ceramics are generally sintered in ambient air atmosphere. However, sintering atmosphere can significantly affect densification behavior at the final stage of sintering [60–63]. For full densification, trapping of insoluble gas inside pores and trapping of pores within grains should be prevented [60–62,64]. If the gas inside the pores is soluble in the ceramic, then the pores can shrink until they disappear and full densification can be achieved [60,61]. For example, porosity in lanthanum-doped PZT could be reduced by sintering in oxygen [65]. Limited work has been carried out on the effect of sintering atmosphere on the sintering behavior and properties of NBT-based ceramics [66–70]. $0.93(Na_{0.5}Bi_{0.5})TiO_3$-$0.07BaTiO_3$ ceramics sintered in oxygen had smaller mean grain size, larger remanent polarization P_r, lower coercivity E_c, higher relative permittivity ε' and larger bipolar electric-field-induced strain than ceramics sintered in nitrogen [66]. The changes in behavior were attributed to a higher concentration of oxygen vacancies in the sample sintered in nitrogen. Sintering in oxygen caused an increase in the relative amount of tetragonal phase for $0.94(Na_{0.5}Bi_{0.5})TiO_3$–$0.06BaTiO_3$ and $0.89(Na_{0.5}Bi_{0.5})TiO_3$–$0.06BaTiO_3$-$0.05BiFeO_3$ compared to sintering in nitrogen [67]. Sintering in oxygen also reduced mean grain size for both compositions, increased P_r for $0.94(Na_{0.5}Bi_{0.5})TiO_3$–$0.06BaTiO_3$ and reduced E_c for $0.89(Na_{0.5}Bi_{0.5})TiO_3$–$0.06BaTiO_3$-$0.05BiFeO_3$. NBT was found to be chemically unstable when sintered in nitrogen, decomposing into $Na_2Ti_6O_{13}$ and an unknown phase [68]. Sintering $0.85(Na_{0.5}Bi_{0.5})TiO_3$–$0.15Ag(Nb_{0.5}Ta_{0.5})O_3$ in oxygen improved electrical breakdown strength and energy storage performance [69]. Sintering in oxygen improved density and reduced mean grain size of $0.66(Bi_{0.5}Na_{0.5})TiO_3$-$0.06BaTiO_3$-$0.28(Bi_xSr_{1-3x/2}\square_{x/2})TiO_3$ samples compared to sintering in air [70]. Samples sintered in oxygen had slimmer polarization hysteresis loops. $0.66(Bi_{0.5}Na_{0.5})TiO_3$-$0.06BaTiO_3$-$0.28(Bi_{0.05}Sr_{0.925}\square_{0.025})TiO_3$ samples sintered in oxygen had slimmer strain hysteresis loops with reduced electric-field-induced strain.

In the present work, the effect of sintering atmosphere (air/oxygen) on densification, grain growth behavior, dielectric, ferroelectric and piezoelectric properties of $0.685\ (Na_{0.5}Bi_{0.5})TiO_3$-$0.065BaTiO_3$-$0.25SrTiO_3$ was investigated. Addition of $SrTiO_3$ to the base NBT-$BaTiO_3$ composition disrupts long-range ferroelectric order, causing a decrease in T_d and T_{FR} to room temperature [28,34,47,58,71]. This composition is in the region of the phase diagram where the room temperature phase changes from a ferroelectric phase to a relaxor phase and behavior shifts from incipient ferroelectric towards electrostrictive [58,59]. This particular composition was chosen as it was expected to have good inverse piezoelectric properties (large high-field inverse piezoelectric constant d_{33}*, low or zero remanent strain, low coercive field E_c and low strain hysteresis η) at relatively low electric field [58,59,72].

2. Materials and Methods

$0.685(Na_{0.5}Bi_{0.5})TiO_3$-$0.065BaTiO_3$-$0.25SrTiO_3$ ceramic powder was prepared via solid-state synthesis. Na_2CO_3 (Acros Organics, Geel, Belgium, 99.5%), $BaCO_3$ (Alfa Aesar, Ward Hill, MA, USA, 99.8%), $SrCO_3$ (Aldrich, St. Louis, MO, USA, 99.9%), TiO_2 (Alfa Aesar, 99.8%) and Bi_2O_3 (Alfa Aesar, 99.9%) were used as starting powders. The starting powders were dried at 250 °C for 5 h before weighing to remove any adsorbed moisture. Stoichiometric amounts of the starting powders were mixed by planetary ball mill (PULVERISETTE 7, Fritsch GmbH, Idar-Oberstein, Germany) in high purity ethanol (Daejung Chemicals, Siheung, Republic of Korea, 99.9%) in ZrO_2-lined grinding jars with ZrO_2 balls of 5 mm diameter as grinding media. The starting powders were milled at 500 rpm for 36 cycles with 5 min operating and 1 min rest for cooling in each cycle. Total milling time was 3 h. After milling, ethanol in the slurry was evaporated using a hot plate/magnetic stirrer. The slurry was put in an oven at 70 °C for 24 h to remove any remaining ethanol. Before and after calcination, the dried powder was crushed in an agate mortar and pestle and sieved through a 180 µm mesh sieve to remove any agglomerates. Calcination is performed at 850 °C for 3 h. Phase formation was checked by X-ray diffraction (XRD, X'Pert PRO, PANalytical, Almelo, The Netherlands). Pellets were made by hand-pressing powder in a 10 mm diameter die, followed by cold isostatic pressing at 40 MPa for 5 min. Samples were sintered in a mini Super Kanthal tube furnace (Adam, Linn High Therm GmbH, Eschenfelden, Germany) at temperatures between 1150 °C and 1250 °C and times between 1 h and 20 h with cooling and heating rates of 5 °C/min under flowing oxygen and air atmospheres with 30 sscm flow rate. Samples were buried in packing powder of the same composition in single alumina crucibles with lids to reduce alkali/bismuth volatilization. Density of the sintered pellets was measured via the Archimedes method in deionized water.

To observe the microstructure, samples were sectioned with a low-speed diamond wheel saw (RB 205 Metsaw-LS, R&B Co., Ltd., Daejeon, Republic of Korea). Samples were ground to a #4000 finish with SiC paper and then polished to a 1 µm finish using diamond suspension. Polished samples were thermally etched for 1 h at a temperature 100 °C below the sintering temperature and Pt coated. Microstructural analysis was performed by scanning electron microscopy (SEM, Hitachi S-4700, Tokyo, Japan). Measurements of grain size (equivalent 2D spherical radius) were made from the micrographs using ImageJ (version 1.50). For the measurements of mean grain size and grain size distribution, at least 400 grains were measured for each sample. Electron probe microanalysis (EPMA, JEOL JXA-8530F PLUS, Tokyo, Japan) was carried out on cross-sections of samples sintered at 1250 °C for 1 h. Samples were ground and polished as before but without thermal etching. Wavelength-dispersive spectroscopy analysis was carried out on carbon-coated samples using $NaAlSi_2O_6$, $Bi_4Ge_3O_{12}$, $BaTiO_3$ and $SrTiO_3$ as standards and with an accelerating voltage of 15 kV.

For dielectric property measurements, both surfaces of the samples were polished to a #4000 SiC finish and cleaned using acetone. Samples were dried in an oven at 70 °C for 1 h prior to applying silver paste electrodes (16032 PELCO, Ted Pella, Redding, CA, USA) on both surfaces. Samples were loaded in a heating/cooling stage (TS1500, Linkam, Tadworth, UK). Measurements were carried out from 30 °C to 700 °C in flowing air. Impedance was measured using an impedance analyzer (HP4284A, Agilent, Santa Clara, CA, USA) from 10^6 Hz to $10^{1.4}$ Hz (=25.1 Hz) at 0.1 intervals in logarithmic frequencies with heating and cooling rates of 1 °C/min.

Polarization and bipolar strain vs. electric field hysteresis loops of samples sintered at 1250 °C for 1 h in air and oxygen were investigated in a commercial apparatus (aixPES, aixACCT Systems GmbH, Aachen, Germany) at 1 Hz under electric fields up to 5 kV/mm. Both surfaces of samples were polished to a #4000 finish with SiC paper. Silver paste electrodes (DS-PF-7472, Daejoo, Siheung, Republic of Korea) were applied on both surfaces and fired at 600 °C for 1 h, with heating and cooling rates of 5 °C/min. Samples were not poled before measurement.

3. Results

An XRD pattern of the calcined $0.685(Na_{0.5}Bi_{0.5})TiO_3$-$0.065BaTiO_3$-$0.25SrTiO_3$ powder is shown in Figure 1. The calcined powder has the perovskite structure without any impurity phase and the XRD pattern could be indexed with COD pattern #96-210-3298 for $(Na_{0.5}Bi_{0.5})TiO_3$ (cubic, space group $Pm\overline{3}m$). XRD patterns of $0.685(Na_{0.5}Bi_{0.5})TiO_3$-$0.065BaTiO_3$-$0.25SrTiO_3$ samples sintered at 1250 °C in air and oxygen are shown in Figure 2. The samples sintered in air and oxygen both have the perovskite structure without any impurity phase and both XRD patterns could be indexed with COD pattern #96-210-3298 for $(Na_{0.5}Bi_{0.5})TiO_3$ (cubic, space group $Pm\overline{3}m$).

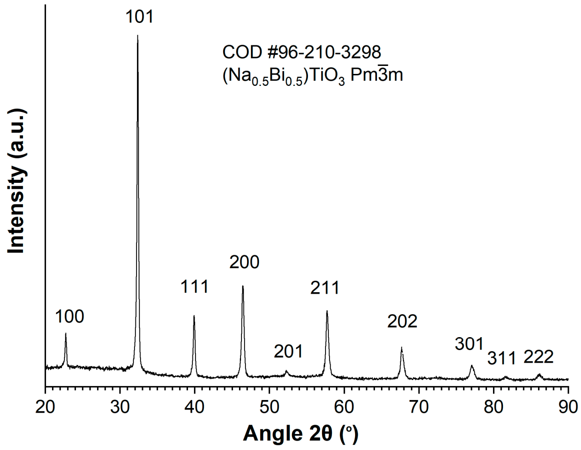

Figure 1. XRD pattern of 0.685($Na_{0.5}Bi_{0.5}$)TiO_3-0.065$BaTiO_3$-0.25$SrTiO_3$ powder calcined at 850 °C for 3 h.

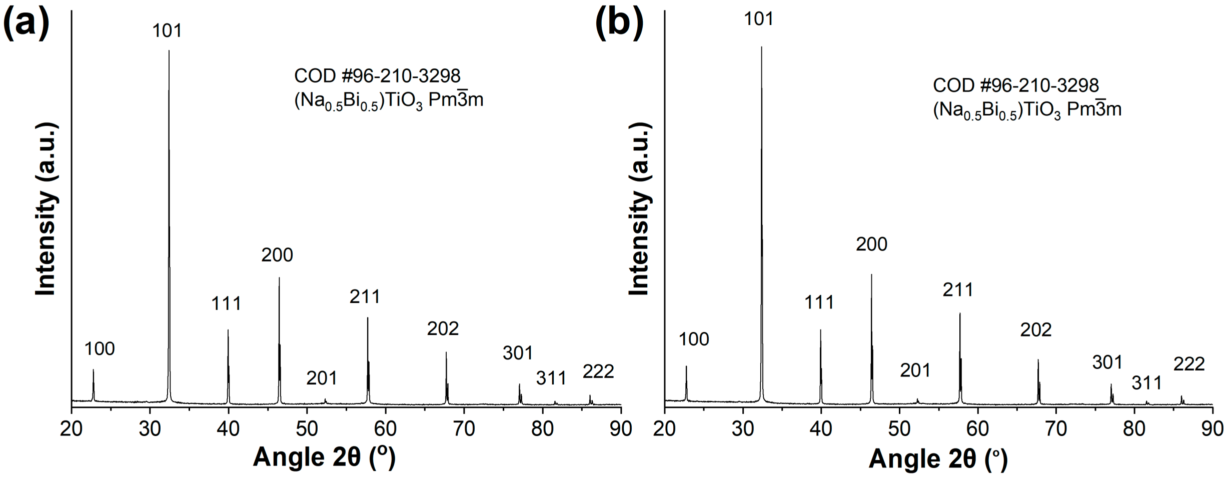

Figure 2. XRD patterns of 0.685($Na_{0.5}Bi_{0.5}$)TiO_3-0.065$BaTiO_3$-0.25$SrTiO_3$ samples sintered at 1250 °C for 1 h in (**a**) air and (**b**) oxygen.

The densification behavior of samples sintered in air and oxygen at temperatures between 1150~1250 °C for 1–20 h is shown in Figure 3. The theoretical density of 0.685($Na_{0.5}Bi_{0.5}$)TiO_3-0.065$BaTiO_3$-0.25$SrTiO_3$ was calculated to be 5.728 g/cm^3 based on unit cell parameters estimated from the XRD pattern of a sintered pellet [72]. Oxygen sintering significantly improves the densification of samples, especially in samples sintered at 1150 °C and 1200 °C. The highest density (99.3% theoretical density) was observed after sintering at 1250 °C for 1 h in oxygen atmosphere. Increasing the sintering temperature causes an increase in density for samples sintered in both air and oxygen. The effect is more pronounced for samples sintered in air, as the samples sintered in oxygen already have densities above 95% theoretical density even at the lower sintering temperatures. The increase in density with sintering temperature in both air and oxygen can be explained by the faster atomic diffusion through the crystal lattice at higher temperatures. The relative density of samples sintered in both air and oxygen at 1150 °C and 1200 °C increases with time and reaches the highest value between 5~10 h, then starts to decrease with further sintering. For samples sintered in both air and oxygen at 1250 °C, maximum density is reached by 1 h sintering, after which point density decreases.

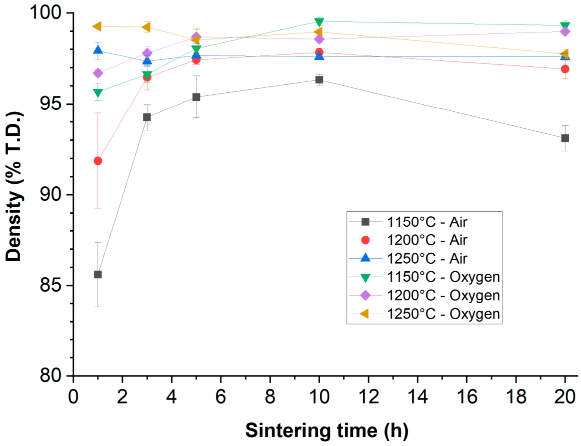

Figure 3. Density values of 0.685($Na_{0.5}Bi_{0.5}$)TiO_3-0.065$BaTiO_3$-0.25$SrTiO_3$ samples sintered in air and oxygen.

SEM micrographs of samples sintered in air and oxygen at temperatures between 1150 and 1250 °C for 1 h are given in Figure 4. There are numerous residual closed pores in the sample sintered at 1150 °C in air [Figure 4a] which indicate incomplete densification. As sintering temperature increases porosity decreases but is still present even at 1250 °C [Figure 4b,c]. In contrast, the samples sintered in oxygen exhibit smaller grain size and fewer and smaller pores than the corresponding samples sintered in air [Figure 4d–f]. SEM micrographs of 0.685($Na_{0.5}Bi_{0.5}$)TiO_3-0.065$BaTiO_3$-0.25$SrTiO_3$ samples sintered in air and oxygen at 1250 °C for 20 h are shown in Figure 5. The sample sintered in oxygen has smaller grains than the sample sintered in air. Neither of the samples appears to show pore/boundary separation. Samples sintered in both air and oxygen show abnormal grain growth. The abnormal grains are cuboid in shape with faceted grain boundaries.

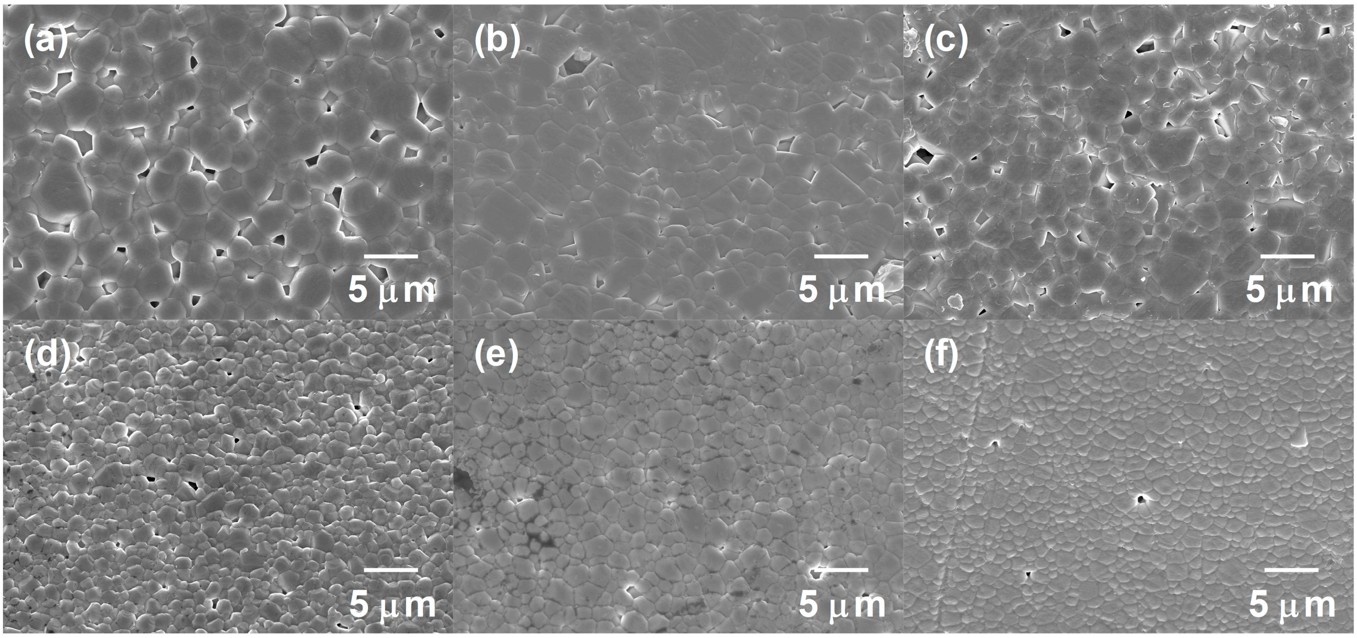

Figure 4. SEM micrographs of 0.685($Na_{0.5}Bi_{0.5}$)TiO_3-0.065$BaTiO_3$-0.25$SrTiO_3$ samples sintered for 1 h in: (**a**) air at 1150 °C; (**b**) air at 1200 °C; (**c**) air at 1250 °C; (**d**) oxygen at 1150 °C; (**e**) oxygen at 1200 °C; (**f**) oxygen at 1250 °C.

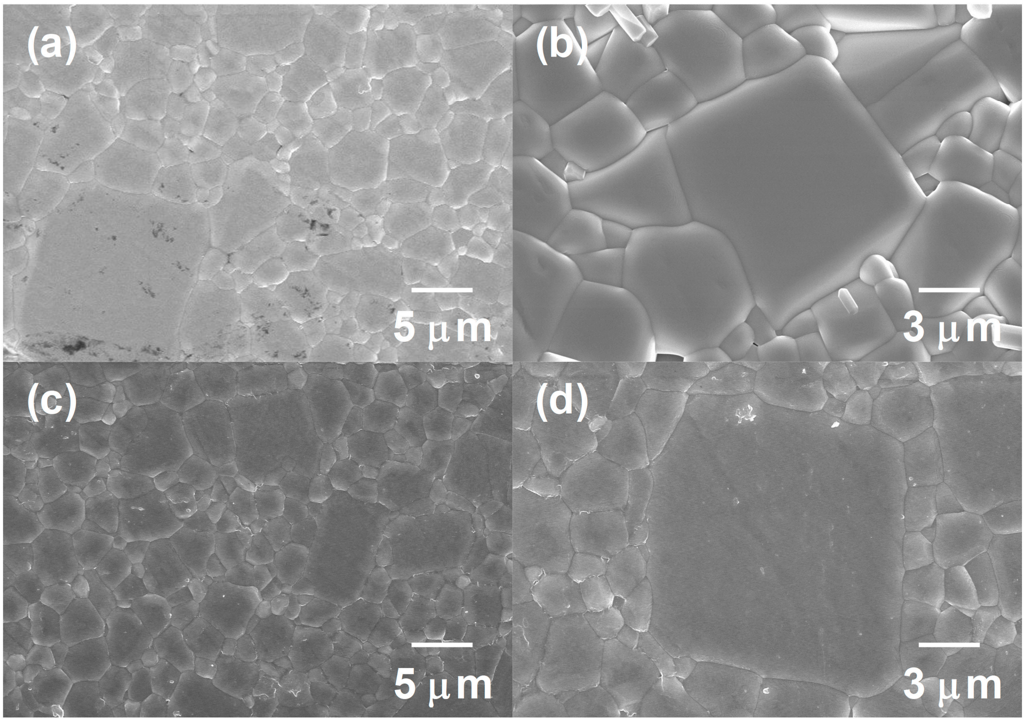

Figure 5. SEM micrographs of 0.685($Na_{0.5}Bi_{0.5}$)TiO_3-0.065$BaTiO_3$-0.25$SrTiO_3$ samples sintered in (**a**,**b**) air and (**c**,**d**) oxygen at 1250 °C for 20 h.

The mean grain size (2D equivalent spherical radius) of the samples sintered between 1150 °C~1250 °C in air or oxygen atmosphere for times up to 20 h is shown in Figure 6. With increased sintering time, the mean grain size increases for all samples irrespective of sintering atmosphere. For the samples sintered in air, increasing the sintering temperature from 1150 to 1200 °C causes a decrease in mean grain size, with a further increase in sintering temperature to 1250 °C not having much effect. For samples sintered in oxygen, increasing the sintering temperature from 1150 to 1200 °C causes an increase in mean grain size for sintering times up to 10 h. Further increasing the sintering temperature to 1250 °C initially has little effect, but mean grain size increases further after sintering for more than 5 h. Sample which are sintered at 1150 °C in air atmosphere have the largest mean grain sizes among all samples. In contrast to this behavior, samples sintered in oxygen at 1150 °C have the lowest mean grain sizes among all the samples. In general, sintering in oxygen inhibits grain growth in the ceramics.

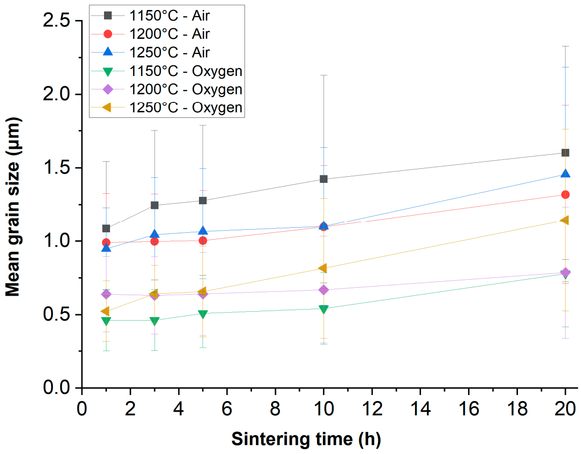

Figure 6. Mean grain size of 0.685($Na_{0.5}Bi_{0.5}$)TiO_3-0.065$BaTiO_3$-0.25$SrTiO_3$ samples sintered in air or oxygen at temperatures between 1150~1250 °C for 1~20 h.

https://doi.org/10.3390/cryst16020143

Sintering trajectory diagrams of the samples sintered between 1150 °C~1250 °C in air or oxygen atmosphere for times up to 20 h are shown in Figure S1. It is seen more clearly in these diagrams that the samples sintered in oxygen at 1150 °C and 1200 °C show less variation in density for samples sintered at a particular temperature and time than the corresponding samples sintered in air, i.e., the error bars representing the standard deviation of density are narrower for the samples sintered in oxygen. For samples sintered at 1250 °C, variation in density does not change much between samples sintered in air and in oxygen. The sintering trajectory of the samples sintered in oxygen shifts to higher densities and smaller mean grain sizes compared to samples sintered in air, particularly for samples sintered at 1150 °C and 1200 °C, which is beneficial for avoiding abnormal grain growth and pore entrapment inside grains [64,73].

The grain size distributions for samples sintered in air at temperatures between 1150 °C and 1250 °C and times up to 20 h are given in Figure 7. At all sintering temperatures, the grain size distributions become broader with increasing sintering time, which is a sign of abnormal grain growth. Abnormal grains are defined as grains of size greater than three times the mean grain size [74]. Somewhat counterintuitively, the grain size distributions at times between 1~10 h become slightly narrower as sintering temperature increases, mirroring the change in mean grain size (Figure 6).

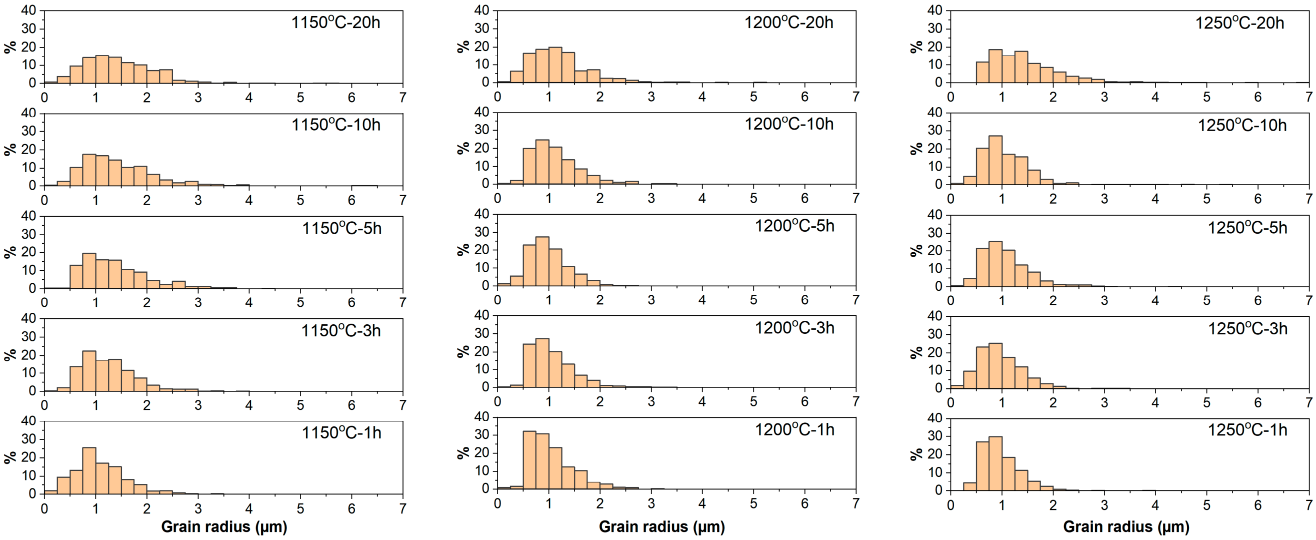

Figure 7. Grain size distributions of 0.685(Na$_{0.5}$Bi$_{0.5}$)TiO$_3$-0.065BaTiO$_3$-0.25SrTiO$_3$ samples sintered in air at temperatures between 1150~1250 °C for 1~20 h.

The grain size distributions for samples sintered in oxygen at temperatures between 1150 °C and 1250 °C and times up to 20 h are given in Figure 8. Narrower grain size distributions are observed in samples sintered in oxygen than in samples sintered in air. In contrast to the grain size distributions of samples sintered at 1150 °C in air, unimodal grain size distributions continue to exist in samples sintered at 1150 °C in oxygen up to 20 h. In samples sintered in oxygen, abnormal grain growth was successfully inhibited at 1150 °C for up to 20 h, compared with samples sintered in air, where abnormal grains appeared after sintering at 1150 °C for only 3 h. The grain size distributions of samples sintered in oxygen broaden more rapidly at 1200 °C and 1250 °C, resulting in abnormal grains of increased number and size after sintering for 10 h. In general, the grain size distributions of samples sintered in oxygen broaden with increasing sintering temperature and time relatively slowly compared to the samples sintered in air.

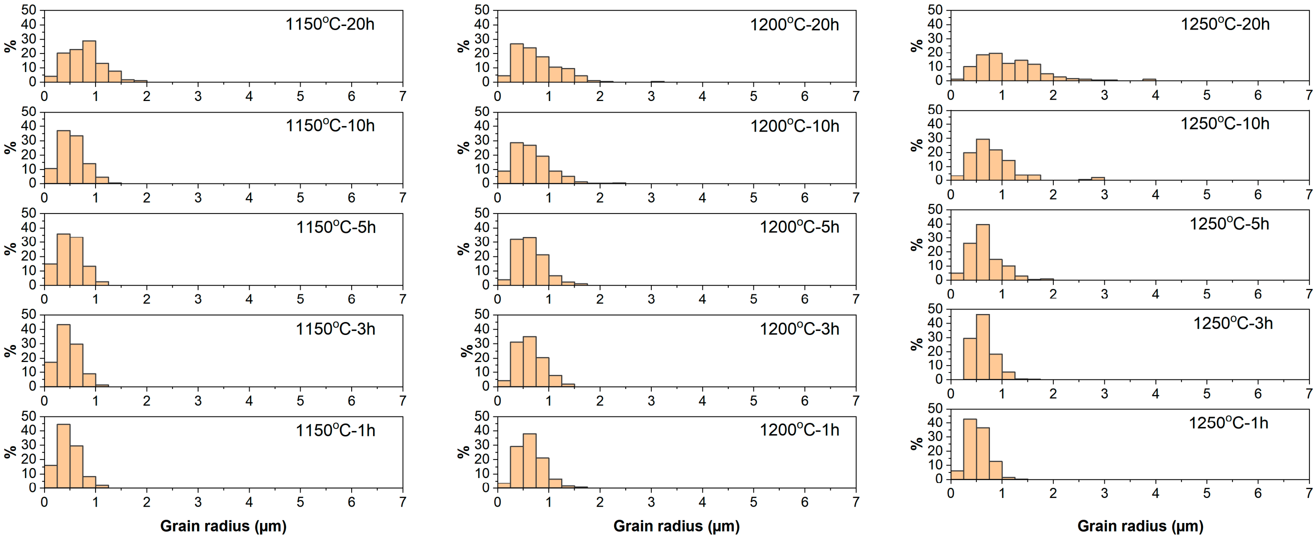

Figure 8. Grain size distributions of 0.685($Na_{0.5}Bi_{0.5}$)TiO_3-0.065$BaTiO_3$-0.25$SrTiO_3$ samples sintered in oxygen at temperatures between 1150~1250 °C for 1~20 h.

The EPMA analysis results of 0.685($Na_{0.5}Bi_{0.5}$)TiO_3-0.065$BaTiO_3$-0.25$SrTiO_3$ samples sintered at 1250 °C for 1 h in air or oxygen are shown in Table 1. Results are presented as the mean and standard deviation of the mol % of each constituent oxide. Ten points were measured for the sample sintered in air and thirteen points for the sample sintered in oxygen. The sample sintered in air is slightly Na-deficient and Bi-excess. The small Na-deficiency and Bi-excess may occur due to Na evaporation [75] during sintering and to maintain charge balance [76], respectively. The sample sintered in oxygen is both Na- and Bi-excess. The Na_2O/Bi_2O_3 ratio was found to be 0.962 and 1.012 for samples sintered in air and oxygen, respectively. The results indicate that the evaporation of Na is lower in samples sintered in an oxygen atmosphere than in samples sintered in air. NBT-based materials commonly have non-stoichiometry problems (Na or Bi deficiency) due to the high temperature sintering process and the volatility of Na and Bi [77,78].

Table 1. EPMA results of 0.685($Na_{0.5}Bi_{0.5}$)TiO_3-0.065$BaTiO_3$-0.25$SrTiO_3$ samples sintered in air and oxygen at 1250 °C for 1 h.

Oxide (Mol %)	Air	Oxygen	Nominal
Na_2O	10.14 ± 0.83	10.94 ± 1.24	10.33
Bi_2O_3	10.54 ± 0.30	10.81 ± 0.54	10.33
TiO_2	60.29 ± 0.95	58.92 ± 2.30	60.33
BaO	3.90 ± 0.28	3.73 ± 0.35	3.92
SrO	15.13 ± 0.90	15.59 ± 0.84	15.08

Figures 9 and 10 show the temperature dependent plots of the real part of the relative permittivity, imaginary part of the relative permittivity and AC conductivity of samples sintered at 1250 °C for 1 h in air or oxygen respectively. Samples were measured during cooling from 700 °C to 30 °C. Data is plotted for selected frequencies of Log(f/Hz) = 5 to 1.5 with intervals of 0.5. The plots of the real part of the relative permittivity show relaxor behavior, with a peak between 90~140 °C which shows frequency dispersion [36]. The peak shifts to higher temperatures and lower values of permittivity as measurement frequency increases. Plots of relative permittivity of NBT-based materials often show two characteristic features, usually labeled T_s and T_m [35,36,58,59,72]. The former (T_s) usually corresponds to a lower temperature where a frequency-dispersive shoulder develops while the latter (T_m) is peak with little frequency dispersion indicating the temperature of maximum relative permittivity. T_s and T_m have been reported to be a ferroelectric–antiferroelectric phase transition and antiferroelectric–paraelectric phase transition respectively [79–81]. Other researchers have suggested that T_s and T_m are related to the transformation of low-temperature rhombohedral (R3c) polar nanoregions into high-temperature tetragonal (P4bm) polar nanoregions [82–84]. If large amounts of components such as $BaTiO_3$ or $SrTiO_3$ are added to NBT, the values of permittivity at T_s increase while the values at T_m decrease [35,85–87]. Eventually the peak at T_m disappears, as can be seen in Figures 9a and 10a. The values of the real part of the relative permittivity at 30 °C are slightly higher for the samples sintered in oxygen. Plots of imaginary relative permittivity vs. temperature in Figures 9b and 10b also show frequency-dispersive peaks at temperatures between 60~100 °C. These peaks are related to the T_s peaks in the plots of real permittivity. As temperature increases above 300 °C, imaginary relative permittivity increases again. In the peaks between 60~100 °C, imaginary relative permittivity increases with measurement frequency due to polarization relaxation, while at higher temperatures imaginary relative permittivity decreases with increasing measurement frequency, indicating that these losses are due to defect conduction [35].

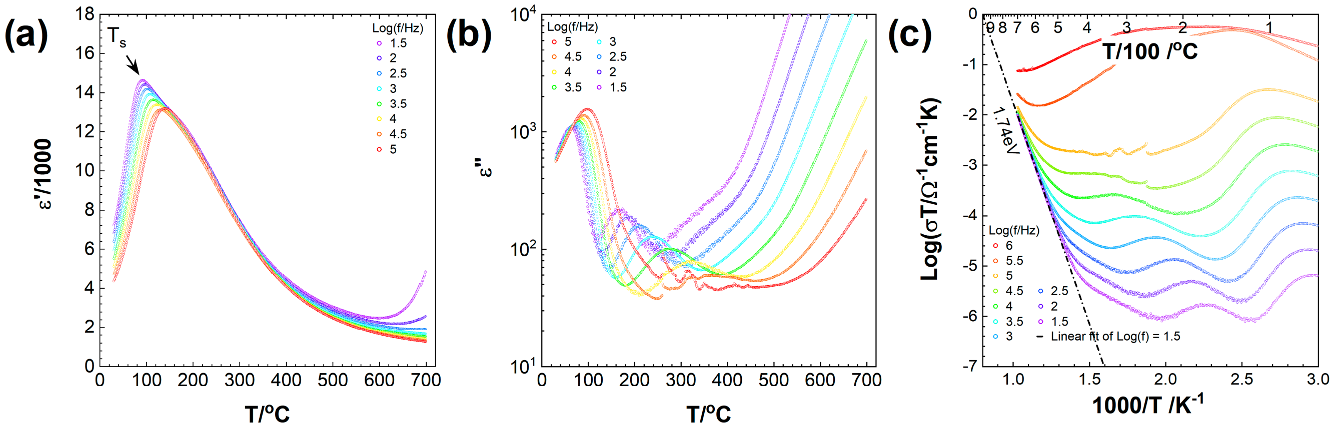

Figure 9. Dielectric and AC conductivity properties at selected frequencies measured on cooling over the temperature range of 700~30 °C of a $0.685(Na_{0.5}Bi_{0.5})TiO_3$-$0.065BaTiO_3$-$0.25SrTiO_3$ sample sintered at 1250 °C for 1 h in air. Temperature dependence plots of: (**a**) real relative permittivity; (**b**) imaginary relative permittivity in logarithmic scale; (**c**) Arrhenius plots of the AC conductivity.

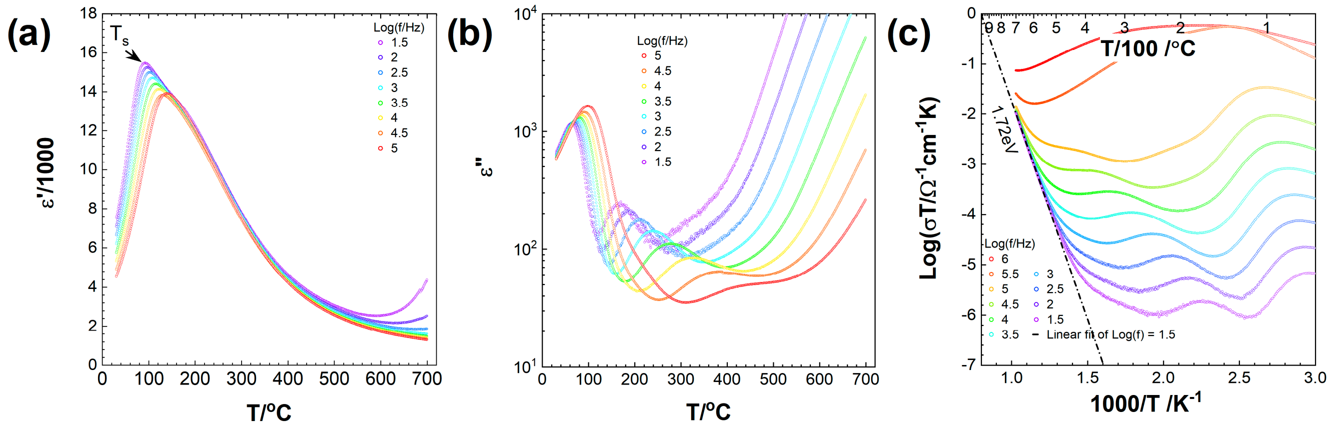

Figure 10. Dielectric and AC conductivity properties at selected frequencies measured on cooling over the temperature range of 700~30 °C of a $0.685(Na_{0.5}Bi_{0.5})TiO_3$-$0.065BaTiO_3$-$0.25SrTiO_3$ sample sintered at 1250 °C for 1 h in oxygen. Temperature dependence plots of: (**a**) real relative permittivity; (**b**) imaginary relative permittivity in logarithmic scale; (**c**) Arrhenius plots of the AC conductivity.

https://doi.org/10.3390/cryst16020143

Plots of log(σT) vs. 1/T are shown in Figures 9c and 10c. Conductivity is plotted as [88,89]:

$$\sigma T = \sigma_0 \exp\left(-\frac{E_a}{kT}\right) \tag{1}$$

where k is the Boltzmann constant 8.617×10^{-5} eV/K and σ_0 is the pre-exponential factor. Based on the slopes of the Arrhenius plots of log(σT) vs. 1/T at a frequency of log(f) = 1.5 and temperatures between 550 °C and 700 °C, activation energies for conduction E_a of 1.74 ± 0.00066 eV and 1.72 ± 0.00151 eV were determined for samples sintered at 1250 °C for 1 h in air and oxygen respectively. Conductivity increases with measurement frequency, indicating promoted hopping of charge carriers [90].

The room temperature bipolar polarization and strain hysteresis loops for $(Na_{0.5}Bi_{0.5})TiO_3$-$0.065BaTiO_3$-$0.25\ SrTiO_3$ samples sintered at 1250 °C for 1 h in air and oxygen atmosphere are shown in Figure 11. The bipolar polarization hysteresis loops show non-linear pinched hysteresis loops for the sample sintered in air, whereas the sample sintered in oxygen shows more linear loops [Figure 11(a1,b1)]. Polarization increases up to an electric field of ~3 kV/mm for the sample sintered in air and then levels off, indicating the completion of the relaxor–ferroelectric phase transition. For the sample sintered in oxygen polarization levels off after an electric field of 4 kV/mm, indicating that the relaxor–ferroelectric phase transition requires larger electric fields. $2P_r$ and $2E_c$ are found to be 6.2 μC/cm^2 and 0.74 kV/mm for the sample sintered in air while they are 8.2 μC/cm^2 and 1.08 kV/mm for the sample sintered in oxygen [Figure 11(c1)]. Samples sintered in air and oxygen both have sprout-shaped bipolar strain curves without negative strain (S_{neg}) [Figure 11(a2,b2)]. S_{neg} is associated with the competition between 180° and non-180° domain switching processes, so S_{neg} increases with increasing non-180° domain switching [16]. Large electric-field-induced strains exist when the macroscopic piezoelectricity nearly disappears and the butterfly shaped strain hysteresis loop of a conventional ferroelectric material transforms to a sprout shape, indicating destabilization of ferroelectricity [16,17,91]. Thus, the addition of $SrTiO_3$ to $(Na_{0.5}Bi_{0.5})TiO_3$-$0.065BaTiO_3$ successfully disrupts the long-range ferroelectric order at room temperature by decreasing T_d and T_{FR} to room temperature, as reported in the literature [58,59]. The maximum electric-field-induced strains are calculated to be 0.13% and 0.14% for samples sintered in air and oxygen, respectively [Figure 11(c2)]. Chen et al. reported that higher remanent polarization, lower coercive field and larger strain were observed for a $0.93(Bi_{0.5}Na_{0.5})TiO_3$-$7BaTiO_3$ sample with smaller grain size sintered in oxygen compared to a sample sintered in nitrogen [66]. Although d_{33}* does not change much in the present work, strain hysteresis is noticeably lower for the sample sintered in oxygen than in air [Figure 11(c2)]. The as-measured electric fields are lower than the nominal electric fields at electric fields > 3 kV/mm, an indication of leakage currents in the samples [92].

Current density-electric field (J-E) curves for samples sintered at 1250 °C for 1 h in air or oxygen are shown in Figure S2. E_{F1} and E_{R1} indicate the formation of an ordered ferroelectric phase from disordered polar nanoregions in an ergodic relaxor phase, and the transition from the ferroelectric phase back to the ergodic relaxor phase, respectively [93–95]. E_{F2} and E_{R2} represent the same phase transitions under reverse/negative electric field [94]. The sample sintered in oxygen exhibits shallower and broader peaks compared to those of the sample sintered in air. In addition, the peaks appear at higher electric fields for the sample sintered in oxygen ($E_{F1} \approx 2.5$ kV/mm for air and $E_{F1} \approx 3.1$ kV/mm for oxygen). This originates from the increased stability of the ergodic relaxor phase, which requires a larger electric field to induce the formation of the ferroelectric phase [96,97]. Peaks E_{R1} and E_{R2} also appear at higher electric fields for the sample sintered in oxygen, implying that the ferroelectric phase is less stable and reverts back to the ergodic relaxor phase more readily than in the sample sintered in air.

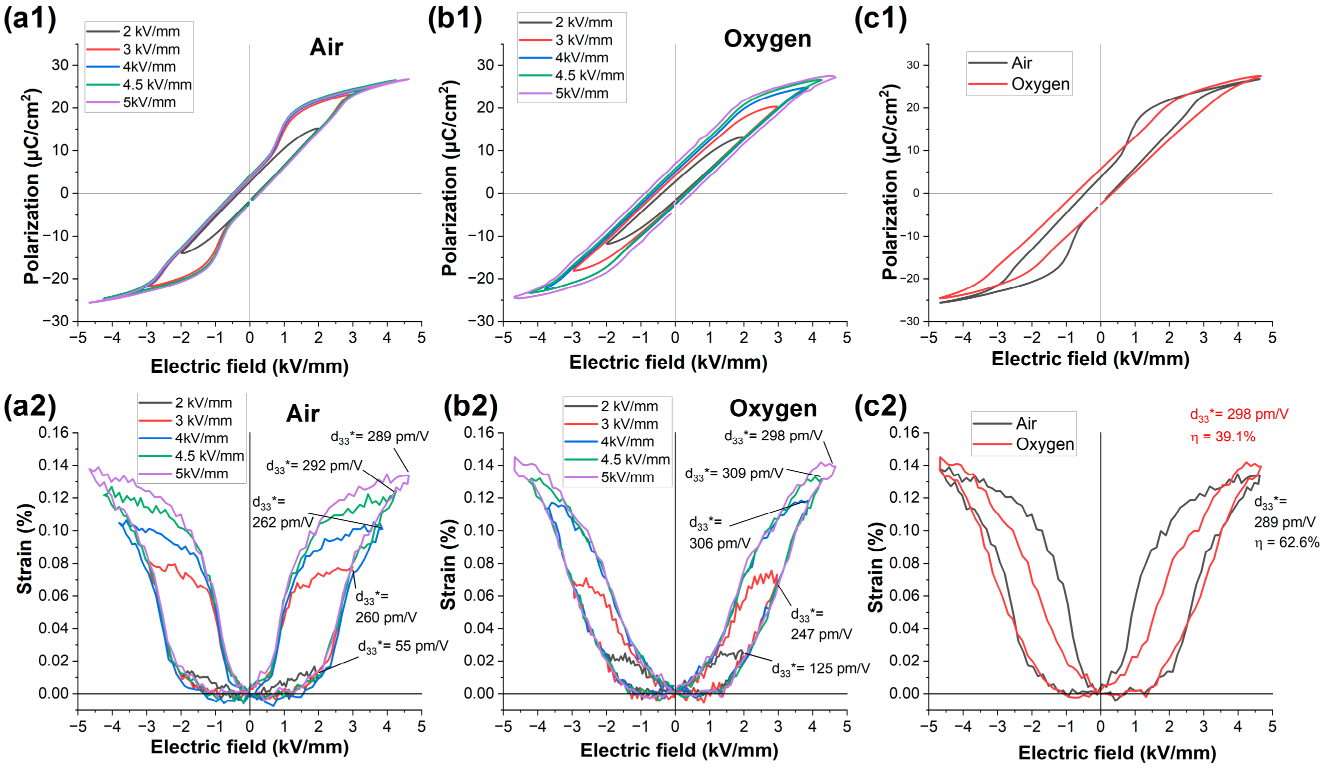

Figure 11. Bipolar polarization and strain hysteresis loops of 0.685($Na_{0.5}Bi_{0.5}$)TiO_3-0.065$BaTiO_3$-0.25$SrTiO_3$ samples sintered at 1250 °C for 1 h in air and oxygen atmospheres: bipolar (**a1**) polarization and (**a2**) strain hysteresis loops of sample sintered in air; bipolar (**b1**) polarization and (**b2**) strain hysteresis loops of sample sintered in oxygen; comparison of (**c1**) polarization and (**c2**) strain hysteresis loops of samples sintered in air and oxygen measured at an electric field of 5 kV/mm.

Previous work on textured ceramics of this composition showed that nominally identical samples could have quite different bipolar polarization and strain hysteresis loops [72]. To check the reproducibility of our results, a second set of samples were sintered at 1250 °C for 1 h in air or oxygen and their hysteresis loops were measured (Figure 12). The results look quite different to those in Figure 11. The sample sintered in air has pinched polarization hysteresis loops as before, but the remnant polarization and coercivity have increased ($2P_r$ = 13.6 μC/cm^2, $2E_c$ = 1.00 kV/mm) compared to the previous sample ($2P_r$ = 5.9 μC/cm^2, $2E_c$ = 0.71 kV/mm) [Figure 12(a1)]. The new sample sintered in oxygen has pinched polarization hysteresis loops [Figure 12(b1)] with reduced remnant polarization and coercivity ($2P_r$ = 5.7 μC/cm^2, $2E_c$ = 0.71 kV/mm) compared to the new sample sintered in air [Figure 12(c1)]. The new sample sintered in oxygen has lower remanent polarization and coercivity compared to the previous sample sintered in oxygen ($2P_r$ = 7.5 μC/cm^2, $2E_c$ = 1.0 kV/mm). The strain hysteresis loop of the new sample sintered in air shows a noticeable negative strain, increased d_{33}* and lower strain hysteresis (59.3% vs. 78.8%) compared to the previous sample sintered in air [Figure 12(a2)]. The negative strain, combined with the increase in remnant polarization and coercivity, suggests that this sample shows more ferroelectric behavior than the previous sample sintered in air. The new sample sintered in oxygen has sprout shaped strain hysteresis loops similar to those of the previous sample sintered in oxygen, but with improved d_{33}* and increased hysteresis (49.9% vs. 41.4%). The new sample sintered in oxygen has lower d_{33}* and hysteresis than the new sample sintered in air [Figure 12(c2)]. The two sets of samples are nominally identical, but different Ag electrodes (SJA-41-257B, Seong-Ji Tech, Uiwang, Republic of Korea) were applied to the new samples as the old electrode paste was no longer available. Possibly the change in electrodes affected the properties, or slight differences in composition. As the composition of the samples is close to the boundary between incipient ferroelectric and electrostrictive behavior [58,59], small changes in composition may have a considerable effect on the electromechanical response. Similar behavior was found for $0.75(Na_{0.5}Bi_{0.5\pm0.01})TiO_3$-$0.25SrTiO_3$ ceramics [98].

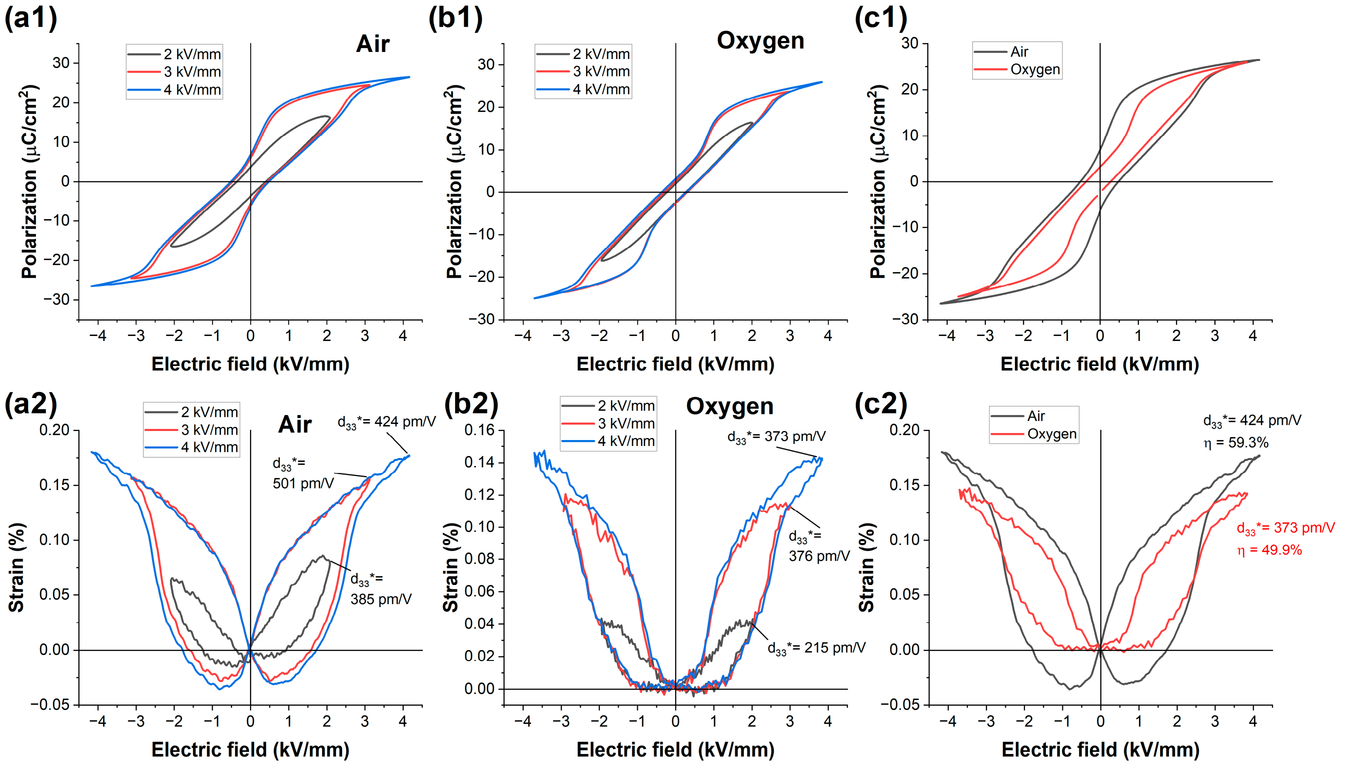

Figure 12. Bipolar polarization and strain hysteresis loops of a second set of $0.685(Na_{0.5}Bi_{0.5})TiO_3$-$0.065BaTiO_3$-$0.25SrTiO_3$ samples sintered at 1250 °C for 1 h in air and oxygen atmospheres: bipolar (**a1**) polarization and (**a2**) strain hysteresis loops of sample sintered in air; bipolar (**b1**) polarization and (**b2**) strain hysteresis loops of sample sintered in oxygen; comparison of (**c1**) polarization and (**c2**) strain hysteresis loops of samples sintered in air and oxygen measured at an electric field of 4 kV/mm.

Current density vs. electric field loops of the second set of samples are shown in Figure S3. The peaks representing the formation of the ferroelectric phase and its transition back to an ergodic relaxor phase are much clearer in the new sample sintered in oxygen than for the previous sample. The ferroelectric phase forms at an electric field of E_{F1} ~ 2.5 kV/mm for new samples sintered both in air and in oxygen. However, the ferroelectric phase reverts back to the relaxor phase at a higher electric field (E_{R1} ~ 0.8 kV/mm) in the sample sintered in oxygen compared to the sample sintered in air (~0.2 kV/mm), again implying that the ferroelectric phase is less stable in the sample sintered in oxygen.

4. Discussion

Sintering the $0.685(Na_{0.5}Bi_{0.5})TiO_3$-$0.065BaTiO_3$-$0.25SrTiO_3$ samples in oxygen improved densification of samples significantly at all temperatures and sintering times compared to sintering in air (Figure 3). Similar results were reported for $0.66(Bi_{0.5}Na_{0.5})TiO_3$-$0.06BaTiO_3$-$0.28(Bi_xSr_{1-3x/2}\square_{x/2})TiO_3$ [70]. Sintering atmosphere significantly affects the densification behavior of powder compacts at the final stage of sintering [60,61]. For full densification, entrapment of insoluble gas inside pores and entrapment of isolated pores within grains should be avoided [64,99,100]. The gas in the sintering atmosphere will be trapped inside the pores when they close and become isolated from the surrounding atmosphere [60,61]. At this point, the pressure of the trapped gas in the pores is equal to the pressure of the sintering atmosphere. There is a driving force for pore shrinkage due to the capillary pressure at the pore surface. As the pore shrinks, the gas pressure inside the pore increases. Once the gas pressure in the pore is equal to the sum of the capillary pressure and the pressure of the sintering atmosphere, the pore can no longer shrink. The diffusivity of the sintering atmosphere gas therefore can determine whether densification is full or limited [60,61,100]. If the gas cannot diffuse through the crystal lattice of the ceramic to the surface (e.g., nitrogen), density will reach a limiting value. If the gas can diffuse through the crystal lattice of the ceramic (e.g., oxygen) then densification can continue as gas pressure in the pores can decrease and the pores can shrink.

Several workers have studied the effect of sintering atmosphere on densification of ceramics. Coble proved that limited densification of alumina occurred during sintering in nitrogen, in contrast to nearly full densification in a hydrogen or oxygen atmosphere [63]. Kim et al. studied the shrinkage behavior of artificially formed large isolated pores in the MgO-$CaMgSiO_4$ system during liquid phase sintering in oxygen and nitrogen [101]. They reported that pore shrinkage occurs by flow of both liquid and grains into the pores when sintering in an oxygen atmosphere while the pores remain stable during sintering in nitrogen, which they explained as being due to the low expected solubility and diffusivity of nitrogen in the liquid phase. Oxygen, on the other hand, can diffuse through the liquid phase, allowing the pores to shrink. Densification of samples without artificially induced pores was also promoted by sintering in oxygen. Therefore, they concluded that liquid-phase sintering in air could be inefficient to remove pores while sintering in oxygen could reduce this problem. The densification rate of MgO-doped Al_2O_3 in the final stage of sintering (above 99% theoretical density) is lower in a non-diffusive atmosphere (nitrogen) than in a diffusive atmosphere (oxygen) [102]. Du et al. reported that higher density was obtained when 95% alumina samples were sintered in pure oxygen gas than when sintered in air [103]. They concluded that the higher solubility and diffusivity of oxygen (compared to nitrogen in air) are beneficial during the final stage of sintering, as the enclosed pores filled with oxygen shrink more easily than those filled with nitrogen gas. Le et al. reported that growing single crystals of $0.75(Na_{0.5}Bi_{0.5})TiO_3$-$0.25SrTiO_3$ by solid-state crystal growth in oxygen improved their density compared to crystals grown in air [75]. The increased density of the $0.685(Na_{0.5}Bi_{0.5})TiO_3$-$0.065BaTiO_3$-$0.25SrTiO_3$ samples sintered in oxygen in the present work shows similar behavior (Figure 3). As well as promoting pore shrinkage in the final stage of sintering, sintering in oxygen leads to a smaller mean grain size (Figure 6). This is also beneficial for densification, as the driving force for densification during the intermediate and final stages of sintering is inversely proportional to mean grain size [61,100].

In the present work, the relative density of the samples increases with time, reaches a maximum value and then levels off or starts to decrease with further sintering. There are several possible reasons for the reduction in density with sintering time. First, the evaporation of Na and/or Bi increases with further sintering time which may cause this behavior. The volatilization of alkali elements (K and Na) and Bi in NBT-based materials is common at high sintering temperatures [104,105]. In many NBT-based studies [106–108], the reason for density reduction when sintering at high temperature or long sintering time is thought to be as a result of alkali or Bi evaporation. Second, during extended sintering in an atmosphere which is partially diffusive, the gas trapped in the pores does not have enough time to reach the sample surface but can diffuse to neighboring pores [63]. The large pores will grow while small pores shrink. Capillary pressure decreases as pore size increases. The large pores can then further expand if the gas pressure in the pore is larger than the sum of capillary pressure and sintering atmosphere pressure [60,63]. The shrinkage of the smaller pores is lower than the expansion of larger pores which results in an increase in overall porosity. This causes a reduction in density and is called bloating [63,64]. Finally, during extended sintering, pore coalescence (merging of smaller pores into larger ones) due to grain growth causes an increase in pore size and bloating [60,64,100,102]. This bloating may be less severe if the gas in the pores can diffuse through the ceramic to the surface, allowing the pores to shrink [60].

Sintering 0.685$(Na_{0.5}Bi_{0.5})TiO_3$-0.065$BaTiO_3$-0.25$SrTiO_3$ samples in oxygen reduced mean grain size (Figure 6) and impeded abnormal grain growth (Figures 7 and 8). Grain growth is usually separated into two types, stationary (normal grain growth) and non-stationary (including abnormal grain growth) [109–111]. In normal grain growth, uniform change occurs in the microstructure, resulting in a relatively narrow unimodal size distribution [109,110]. It is also called stationary grain growth because the relative grain size distribution remains mostly unchanged with sintering time. Abnormal grain growth is based on the consumption of a majority of grains that are not growing or barely growing by a small number of rapidly growing grains [64,109–111]. Unlike normal grain growth, the relative grain size distribution in abnormal or non-stationary grain growth is time-variant and can be very broad or bimodal [109,110]. Upon extended annealing, abnormal grains can impinge and the relative grain size distribution can become unimodal again [110].

Grain growth in the presence of a liquid phase (Ostwald ripening) has been explained by Lifshitz, Slyozov and Wagner (LSW) theory, which describes two mechanisms, diffusion-controlled growth and interface reaction-controlled growth [112,113]. LSW theory predicts a stationary grain size distribution without any abnormal grain growth for both mechanisms. However, the theory assumes a constant solid/liquid interface mobility which is invariant with driving force for grain growth or crystallographic orientation of the surface of the grain. This is valid for macroscopically rounded grains with atomically rough interfaces, in which case grain growth is diffusion controlled [110,114]. LSW theory does not apply to macroscopically faceted grains where solid/liquid interface mobility can change with driving force for grain growth and crystallographic orientation of the grain surface. Therefore, it cannot explain abnormal grain growth [115]. To explain non-stationary grain growth, especially abnormal grain growth, many mechanisms and models have been developed such as the mixed control mechanism of boundary migration [110,116,117], second phase particle (or pore) drag mechanisms [73,118–120], liquid film and complexion mechanisms [121–123] and the solute drag mechanism [124]. The mixed control mechanism is based on the grain growth rate being limited by either diffusion of atoms through the liquid phase between shrinking and growing grains or by attachment (interface reaction) of transported atoms onto the growing grain‘s surface [109,116,117]. The limiting mechanism, diffusion or interface reaction, in turn depends on the atomic structure of the solid/liquid interface.

For a system with solid/liquid interfaces, the driving force Δg for growth of a particular grain is [109,110]:

$$\Delta g = 2\gamma V_m \left(\frac{1}{r^*} - \frac{1}{r} \right) \tag{2}$$

where γ is solid/liquid interfacial energy, V_m is molar volume, r is the grain size (or the distance from the grain center to a facet for faceted grains), and r^* is the radius of a grain which is neither growing nor shrinking (usually the mean grain size). If $\Delta g > 0$ the grain may possibly grow, if $\Delta g < 0$ the grain will shrink and if $\Delta g = 0$ the grain neither grows nor shrinks [109]. The mixed control mechanism of boundary migration is based on grain growth being governed by the coupling of the critical driving force for growth Δg_c (the driving force at which the controlling mechanism transitions between interface reaction control and diffusion control) and the maximum driving force Δg_{max}, the driving force for growth of the largest grain in the microstructure [109,116,117].

The relationship between grain growth rate and driving force Δg for ordered and disordered interfaces is shown in Figure 13 [125]. This relationship depends on the structure of the solid/liquid interface, which can be atomically rough or faceted [109,110,117]. If the system has isotropic solid/liquid interfacial energy, the solid/liquid interfaces are disordered (rough) on an atomic scale and the macroscopic shape of the grains is rounded. Owing to the disordered interface, atoms can attach to many sites on the grain surface and grain growth is limited by the rate at which atoms diffuse to the surface. All grains which have $\Delta g > 0$ will grow (the gray dashed line in Figure 13) and abnormal grains do not form [109,110,116].

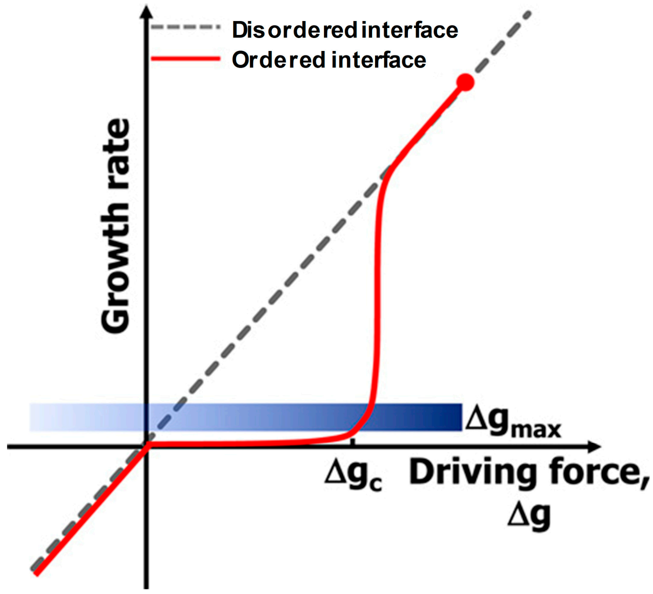

Figure 13. Grain growth rate vs. driving force Δg for disordered and ordered solid/liquid interfaces [125]. Reproduced with permission from S. J. L. Kang, J. H. Park, S. Y. Ko and H. Y. Lee, Journal of the American Ceramic Society; published by John Wiley & Sons, 2015. © 2015 The American Ceramic Society.

For systems with anisotropic solid/liquid interfacial energy, the solid/liquid interfaces will be ordered with flat or terraced surfaces on the atomic scale and the macroscopic shape of the grains will be faceted. Atoms trying to attach to the grain surface will be unstable because of a large number of broken bonds. In order for atoms to stably attach to the grains, favorable low-energy kink-generating sites must be present, e.g., 2D nuclei [126,127] or screw dislocations [127,128]. If the system has ordered solid/liquid interfaces, the migration kinetics are non-linear or linear depending on whether Δg is smaller or larger than the critical driving force Δg_c (the red line in Figure 13 which shows the case for growth controlled by 2D nucleation) [109,110,116]. In the case of $\Delta g < \Delta g_c$, few stable 2D nuclei form on the faceted grain surface [126,129]. The attachment of atoms to the grain is limited due to the lack of low-energy kink sites, resulting in very low grain growth rates [109]. At $\Delta g \geq \Delta g_c$, the rate at which stable 2D nuclei form increases exponentially [126,129]. Many low-energy kink sites now exist so growth is now limited by the rate of diffusion of atoms to the surface and the grain growth rate increases linearly with Δg.

Hence a system with faceted solid/liquid interfaces contains three types of grain:

1. If $\Delta g < 0$, the grain will shrink by diffusion control.

2. If $0 < \Delta g < \Delta g_c$, the growth rate is governed by interface reaction and is very slow.
3. If $\Delta g_c \leq \Delta g \leq \Delta g_{max}$, the growth rate is governed by diffusion and the grain can grow.

The mixed control theory classifies grain growth behavior into four categories based on the relationship between Δg_c and Δg_{max} [109,116,125]:

1. $\Delta g_c = 0$: growth and dissolution of grains are diffusion-controlled and normal grain growth takes place.
2. $0 < \Delta g_c << \Delta g_{max}$: many grains have $\Delta g \geq \Delta g_c$ and grow by diffusion control. This is called pseudo-normal grain growth.
3. $\Delta g_c \approx \Delta g_{max}$: most grains have $\Delta g < \Delta g_c$ and hardly grow. A small number of grains have $\Delta g \geq \Delta g_c$ and can grow, forming abnormal grains.
4. $\Delta g_c >> \Delta g_{max}$: grain growth barely occurs owing to none of the grains having $\Delta g \geq \Delta g_c$. Such growth behavior is called stagnant grain growth.

The critical driving force Δg_c is given by [109,110,116,129]:

$$\Delta g_c = \frac{\pi \sigma_s^2}{kTh} \frac{1}{\ln \Psi n_0} \quad (3)$$

where k is the Boltzmann constant, T is the absolute temperature, $\Psi = n^* v \exp(-\Delta g_m / kT)$, n^* is the number of atoms close to a critical 2D nucleus, v is the vibration frequency of atoms in the liquid, Δg_m is the activation energy for jumping across the liquid/solid interface, h is the height of the 2D nucleus and σ_s is the step free energy.

As seen in Equation (3), Δg_c has a quadratic relationship with σ_s. Step free energy σ_s is affected by sintering atmosphere, composition, dopant addition and sintering temperature [110,127,130–137]. With increasing sintering temperature, the concentration of intrinsic defects, kinks and vacancies increases [130,138–140]. This increases configurational entropy which results in a reduction in σ_s and Δg_c [109,127,138,141]. The maximum driving force (Δg_{max}) depends on the initial grain size distribution and the mean grain size (Equation (2)), so it can vary with sintering time [74,109]. Although the above discussion concerns systems with a liquid phase, similar behavior is observed in solid-state sintered systems [125,129,142–144]. In addition $(Na_{0.5}Bi_{0.5})TiO_3$-based systems often contain small amounts of a liquid phase at the triple junctions during sintering, even if no liquid phase sintering aid is added [74,145,146]. For diffusion-controlled grain growth in systems with a small amount of liquid phase, growth is controlled by movement of the solid/liquid interfaces at the triple junctions [74,147].

Figure 7 shows the grain size distributions of samples sintered in air at 1150~1250 °C for 1 to 20 h. Since all samples were prepared from the same batch of powder, the value of Δg_{max} for all samples should be equal at the beginning of sintering [133]. The other parameter, Δg_c, can be affected by the step free energy [109]. Step free energy can be qualitatively estimated from the macroscopic grain shape [141,148]. Grains with spherical shapes, cubic shapes with round corners and edges and cubic shapes with sharp corners and edges have zero, intermediate and high step free energy, respectively [141,148,149]. The samples in the present work show cuboid grains with rounded corners and edges, especially the abnormal grains (Figure 5). The abnormal grains are expected to show the equilibrium growth shape of the grains because they have grown more than the matrix grains. Le et al. reported that cubic grains with flat faces and rounded edges and corners exist in the $(Na_{0.5}Bi_{0.5})TiO_3$-$SrTiO_3$ system which indicate moderate values of step free energy [141,146,148]. Moon et al. reported cubic grains with faceted and rounded corners in $0.95(Na_{0.5}Bi_{0.5})TiO_3$-$0.05BaTiO_3$ [74]. Therefore, it can be concluded that there is a tendency in $(Na_{0.5}Bi_{0.5})TiO_3$-based systems towards pseudo-normal grain growth at the beginning of sintering due to the low value of Δg_c and the high values of Δg caused by the use of fine powder [74,150].

For the samples sintered at 1150 °C in air, many grains initially have $\Delta g \geq \Delta g_c$, resulting in pseudo-normal grain growth. With further sintering time, the mean grain size increases from 1.08 µm at 1 h to 1.60 µm at 20 h. A large number of grains grow in pseudo-normal grain growth, which results in an increase in mean grain size. The increase in mean grain size causes a reduction in values of Δg for all grains (Equation (2)) [74,109]. As mean grain size increases, the driving force of the majority of grains will fall below Δg_c, their growth behavior will change from diffusion-controlled to interface reaction-controlled and their growth rate will decrease [74,109]. A few grains which are large enough to still have $\Delta g \geq \Delta g_c$ continue to grow and form abnormal grains by consuming smaller grains [74,109]. Therefore, the grain growth changes from pseudo-normal to abnormal grain growth. With further sintering up to 20 h, the grain size distribution becomes broader as the sizes of the abnormal grains increase.

Further increasing sintering temperature to 1200 °C is expected to reduce the step free energy and critical driving force [109,127,138,141]. Therefore, the difference between maximum driving force (Δg_{max}) and critical driving force (Δg_c) is larger now than at 1150 °C. This leads to a delay in the change in grain growth from pseudo-normal to abnormal [146]. Similar to previous studies, therefore, it can be concluded that there is a tendency in $(Na_{0.5}Bi_{0.5})TiO_3$-based systems for pseudo-normal grain growth at the beginning of sintering which changes to abnormal grain growth with longer sintering time and higher temperature [74,150]. Figure 6 shows that average grain size at 1200 °C decreases compared to the average grain size at 1150 °C. In contrast to the samples sintered at 1150 °C, there are now more matrix grains able to grow and compete for material due to the lower critical driving force Δg_c at 1200 °C. So, it will limit the grain growth rate for the matrix grains. This explains why the average grain size at 1200 °C is smaller than at 1150 °C.

Based on the above discussion, it is expected that there would be a further delay in transformation from pseudo-normal to abnormal grain growth in samples sintered at 1250 °C due to the lower critical driving force. However, abnormal grains appeared earlier in samples sintered at 1250 °C, compared as 1200 °C. Phan et al. also observed similar behavior in NBT-ST [146]. They explained that the reduction in the critical driving force with increased temperature is offset by an increase in the solubility and diffusion coefficient of the solid phase in the liquid, both of which promote grain growth [151]. This leads to rapid grain growth and causes grain growth to shift from pseudo-normal to abnormal after only 1 h sintering.

The volatilization of alkali elements (K and Na) and Bi in NBT-based materials is common at high sintering temperatures [104,105]. Volatilization of A site elements during sintering also causes formation of oxygen vacancies to compensate for the charged A-site vacancies, as shown in Equations (4) and (5) [152,153]. Oxygen vacancies can also be formed as shown in Equation (6) [90].

$$2Na_{Na}^{x} + O_{O}^{x} \rightarrow 2Na + \frac{1}{2}O_2 + 2V_{Na}' + V_{\ddot{O}} \tag{4}$$

$$2Bi_{Bi}^{x} + 3O_{O}^{x} \rightarrow 2Bi + \frac{3}{2}O_2 + 2V_{Bi}''' + 3V_{\ddot{O}} \tag{5}$$

$$O_{O}^{x} \rightarrow \frac{1}{2}O_2 + V_{\ddot{O}} + 2e' \tag{6}$$

For the samples sintered in oxygen (P_{O2} = 1 atm), defect reactions (4–6) will be suppressed. As a result, it is expected that the relatively low vacancy concentration will result in higher step free energy and critical driving force [133,154]. In oxygen, the grain growth behavior in the sample sintered at 1150 °C for 1 h is apparently stagnant grain growth (Figure 8). All grains have $\Delta g << \Delta g_c$, so grain growth is very slow due to availability of only a few kink sites on the grains for atoms to attach to during interface reaction-controlled growth. The mean grain size increased from 0.46 µm to 0.78 µm between 1 h~20 h. The unimodal grain size distribution was maintained at 1150 °C for up to 20 h and abnormal grains did not appear. With the increase in the sintering temperature to 1200 °C, Δg_c is expected to decrease due to the increasing concentration of intrinsic defects [130,138–140]. The grain growth behavior is initially stagnant, but with further sintering time, some of the grains grow large enough to have $\Delta g \geq \Delta g_c$ and then grow rapidly to form abnormal grains. The abnormal grains appear after 10 h. With further sintering, the abnormal grain size increases and results in broader grain size distributions. As sintering temperature increases further to 1250 °C, Δg_c decreases further. Although the incubation time needed for abnormal grain growth does not appear to change, abnormal grain growth becomes more prominent when it takes place. It is reported that the incubation time needed for abnormal grain growth increased when oxygen partial pressure of the sintering atmosphere increases [133,154].

Band gaps (E_g) of 3.3 eV [155], 3.25 eV [156] and 3.20 eV [157] are reported for pure NBT, pure ST and pure BT, respectively. From plots of log(σT) vs. 1/T, the activation energies of both $0.715(Na_{0.5}Bi_{0.5})TiO_3$-$0.065BaTiO_3$-$0.22SrTiO_3$ samples were determined to be approximately half the band gap of NBT [Figures 9c and 10c]. It is reported that intrinsic electronic conduction becomes dominant when E_g~$2E_a$ [158,159]. Yang et al. reported that NBT shows three types of electrical behavior, such as oxide ion conduction, mixed ionic–electronic conduction and predominantly electronic conduction subject to various defect mechanisms [78]. They reported that Bi-deficient NBT exhibits oxide ion conductivity while Bi-excess NBT shows electronic conduction with an activation energy of ~1.6 eV. Li et al. reported that non-stoichiometry in NBT significantly affects the activation energies and conduction behavior of samples [77]. They observed that an Na-excess sample has an activation energy less than 1 eV and shows oxide ion conduction while an Na-deficient sample has an activation energy of ~1.7 eV with intrinsic electronic conduction. Hao et al. reported that observation of higher E_a in their samples may result from a decreasing concentration of oxygen vacancies [160]. Steiner et al. reported that the activation energy of pure NBT varies from 0.92 eV to 1.54 eV with increasing temperature due to change from extrinsic semiconducting behavior at low temperature to intrinsic semiconducting behavior at high temperature, where an activation energy almost equal to half the band gap value was observed [161]. Li et al. reported that the activation energy of undoped NBT was observed be less than 0.9 eV while the activation energy of 0.5–1 wt% Nb-doped NBT was observed to be 1.5~1.8 eV [162]. Le et al. reported that the activation energy at high temperature was found to be 1.65 eV for $0.75(Na_{0.5}Bi_{0.5})TiO_3$-$0.25SrTiO_3$ polycrystal samples, approximately half the value of the band gap [163].

There are different values of activation energy reported for NBT-based materials depending on several factors such as the analysis temperature range, doping effect, non-stoichiometry, and concentration of oxygen vacancies as discussed above [77,90,161–163]. There are three possible conduction mechanisms in NBT single crystals depending on the temperature [90,164]: at low temperatures up to ~200 °C, the conduction mechanism is intrinsic electronic conduction; between 200~350 °C, conduction is attributed to small polaron hopping and eventually singly ionized oxygen vacancies; above T_m, an increase in E_a indicates that conduction occurs by a combination of intrinsic free electrons and movement of oxygen vacancies. Doubly ionized oxygen vacancies are dominant in the higher temperature range instead of singly ionized oxygen vacancies.

In the present work, the values of conduction activation energy E_a at high temperature are ~1.7 eV, approximately half the value of the band gap, indicating that intrinsic conduction takes place [77,78,161]. The value of conduction activation energy E_a was slightly lower in the sample sintered in oxygen compared to the sample sintered in air. This may be due to the lower concentration of oxygen vacancies in the sample sintered in oxygen. During cooling, the oxygen vacancies formed by Equations (4)–(6) can be removed according to [78,153]:

$$\frac{1}{2}O_2(g) + V_O^{\cdot\cdot} \rightarrow O_O^{x} + 2h^{\cdot} \quad (7)$$

Some of the electron holes formed by this reaction will eliminate the free electrons formed in Equation (6), but some will be available for conduction [165]. Sintering the sample in oxygen may therefore cause an increase in p-type conductivity by increasing the concentration of electron holes.

The polarization hysteresis loops of the samples show the pinched shape characteristic of incipient ferroelectric materials [16,17,20]. A metastable ferroelectric phase forms when a sufficiently high electric field is applied and reverts back to a nonpolar phase upon removal of the field [20,91,166]. This also leads to the characteristic sprout-shaped bipolar strain hysteresis loop with very small or zero remanent strain, as the material changes between a cubic or pseudocubic nonpolar phase and a noncubic ferroelectric phase [16]. Oxygen vacancies are generally considered to pin non-180° ferroelectric domain walls and retard their movement, hence acting as an obstacle to polarization switching [153,167–169]. In the air-sintered samples, the higher concentration of oxygen vacancies pins the domain walls, stabilizing the metastable ferroelectric phase that has formed under the influence of the electric field. The ferroelectric phase reverts back to the nonpolar phase at a lower electric field than in the oxygen-sintered samples. This accounts for the increased strain hysteresis in the air-sintered samples (Figures 11 and 12) and the shifting of peaks E_{R1} and E_{R2} to lower electric fields in the polarization current density hysteresis loops (Figures S2 and S3).

5. Conclusions

The effect of sintering parameters, including atmosphere (air/oxygen), temperature (1150 °C~1250 °C) and holding time (1~20 h) on the sintering behavior and electrical properties of $0.685(Na_{0.5}Bi_{0.5})TiO_3$-$0.065BaTiO_3$-$0.25SrTiO_3$ electroceramics was investigated. Sintering in oxygen was found to be an effective method to achieve smaller grain size and higher density for $0.685(Na_{0.5}Bi_{0.5})TiO_3$-$0.065BaTiO_3$-$0.25SrTiO_3$ electroceramics, compared with air sintered samples. Sintering in oxygen allows easier pore shrinkage and removal at the final stage of sintering, as oxygen trapped in closed pores can diffuse more readily through the crystal lattice than nitrogen. Reduced vacancy concentration in the oxygen-sintered samples results in higher step free energy and critical driving force for grain growth, retarding grain growth and abnormal grain growth. It was found that $0.685(Na_{0.5}Bi_{0.5})TiO_3$-$0.065BaTiO_3$-$0.25SrTiO_3$ electroceramics sintered at 1250 °C for 1 h in oxygen exhibit smaller grain size, higher density, similar d_{33}* and lower strain hysteresis compared to samples sintered in air. The lower strain hysteresis is caused by the reduced stability of the metastable electric-field-induced ferroelectric phase due to the lower concentration of domain wall-pinning oxygen vacancies. This allows the ferroelectric phase to revert back to the nonpolar phase more easily upon removal of the electric field.

Supplementary Materials: The following supporting information can be downloaded at: https://www.mdpi.com/article/10.3390/cryst16020143/s1, Figure S1: Sintering trajectory diagrams of $0.685(Na_{0.5}Bi_{0.5})TiO_3$-$0.065BaTiO_3$-$0.25SrTiO_3$ samples sintered in (a) air and (b) oxygen at temperatures between 1150~1250 °C for 1~20 h; Figure S2: Current density loops of $0.685(Na_{0.5}Bi_{0.5})TiO_3$-$0.065BaTiO_3$-$0.25SrTiO_3$ samples sintered at 1250 °C for 1h in (a) air and (b) oxygen atmospheres; Figure S3: Current density loops of a second set of $0.685(Na_{0.5}Bi_{0.5})TiO_3$-$0.065BaTiO_3$-$0.25SrTiO_3$ samples sintered at 1250 °C for 1 h in (a) air and (b) oxygen atmospheres.

Author Contributions: Conceptualization, N.E., J.G.F.; methodology, J.G.F., J.-S.L.; formal analysis, N.E., J.G.F.; investigation, N.E., T.T.H.T., W.-J.C., Y.-B.H.; resources, J.G.F., J.-S.L., W.J.; data curation, N.E., J.G.F.; writing—original draft preparation, N.E.; writing—review and editing, J.G.F., T.T.H.T., J.-S.L., W.-J.C., Y.-B.H., W.J.; visualization, N.E., J.G.F., J.-S.L.; supervision, J.G.F., J.-S.L., W.J.; project administration, J.G.F., J.-S.L.; funding acquisition, J.G.F., J.-S.L. All authors have read and agreed to the published version of the manuscript.

Funding: This study was supported by a National Research Foundation of Korea (NRF) grant funded by the Korean government (MSIT) (Grant No. 2021R1F1A1046778). Jong-Sook Lee was supported by a National Research Foundation of Korea (NRF) grant funded by the Ministry of Science and ICT (MSIT) (Grant No. NRF-2018R1A5A1025224).

Data Availability Statement: The original contributions presented in the study are included in the article; further inquiries can be directed to the corresponding authors.

Acknowledgments: The authors would like to thank Jung-Yeol Park and Kyeong-Kap Jeong (Centre for Research Facilities, Chonnam National University) for operating the EPMA and XRD respectively, and Hye-Jeong Kim (Centre for Development of Fine Chemicals, Chonnam National University) for operating the SEM.

Conflicts of Interest: The authors declare no conflicts of interest. The funders had no role in the design of the study; in the collection, analyses, or interpretation of data; in the writing of the manuscript; or in the decision to publish the results.

References

1. Li, F.; Wang, B.; Gao, X.; Damjanovic, D.; Chen, L.Q.; Zhang, S. Ferroelectric materials toward next-generation electromechanical technologies. *Science* **2025**, *389*, eadn4926. [CrossRef]
2. Qiu, C.; Wang, B.; Zhang, N.; Zhang, S.; Liu, J.; Walker, D.; Wang, Y.; Tian, H.; Shrout, T.R.; Xu, Z.; et al. Transparent ferroelectric crystals with ultrahigh piezoelectricity. *Nature* **2020**, *577*, 350–354. [CrossRef]
3. Hales, A.; Jiang, X. A review of piezoelectric fans for low energy cooling of power electronics. *Appl. Energy* **2018**, *215*, 321–337. [CrossRef]
4. Hou, J.F.; Nayeem, M.O.G.; Caplan, K.A.; Ruesch, E.A.; Caban-Murillo, A.; Criado-Hidalgo, E.; Ornellas, S.B.; Williams, B.; Pearce, A.A.; Dagdeviren, H.E.; et al. An implantable piezoelectric ultrasound stimulator (ImPULS) for deep brain activation. *Nat. Commun.* **2024**, *15*, 4601. [CrossRef] [PubMed]
5. Liu, J.; Tan, H.; Zhou, X.; Ma, W.; Wang, C.; Tran, N.-M.-A.; Lu, W.; Chen, F.; Wang, J.; Zhang, H. Piezoelectric thin films and their applications in MEMS: A review. *J. Appl. Phys.* **2025**, *137*, 020702. [CrossRef]
6. Yuan, X.; Shi, J.; Kang, Y.; Dong, J.; Pei, Z.; Ji, X. Piezoelectricity, Pyroelectricity, and Ferroelectricity in Biomaterials and Biomedical Applications. *Adv. Mater.* **2024**, *36*, 2308726. [CrossRef] [PubMed]
7. Gao, X.; Yang, J.; Wu, J.; Xin, X.; Li, Z.; Yuan, X.; Shen, X.; Dong, S. Piezoelectric Actuators and Motors: Materials, Designs, and Applications. *Adv. Mater. Technol.* **2020**, *5*, 1900716. [CrossRef]
8. Uchino, K. *Ferroelectric Devices*; CRC Press: Boca Raton, FL, USA, 2018.
9. Ringgaard, E.; Wurlitzer, T. Lead-free piezoceramics based on alkali niobates. *J. Eur. Ceram. Soc.* **2005**, *25*, 2701–2706. [CrossRef]
10. The European Parliament and The Council of The European Union. Directive 2002/96/EC of the European Parliament and of the Council of 27 January 2003 on waste electrical and electronic equipment (WEEE). *Off. J. Eur. Union* **2003**, *L37*, 24–38.
11. Fan, P.; Liu, K.; Ma, W.; Tan, H.; Zhang, Q.; Zhang, L.; Zhou, C.; Salamon, D.; Zhang, S.T.; Zhang, Y.; et al. Progress and perspective of high strain NBT-based lead-free piezoceramics and multilayer actuators. *J. Mater.* **2021**, *7*, 508–544. [CrossRef]
12. The European Parliament and The Council of The European Union. Restriction of the use of certain hazardous substances in electrical and electronic equipment (RoHS). *Off. J. Eur. Communities* **2013**, *46*, 19–23.

13. Rödel, J.; Jo, W.; Seifert, K.T.P.; Anton, E.M.; Granzow, T.; Damjanovic, D. Perspective on the Development of Lead-free Piezoceramics. *J. Am. Ceram. Soc.* **2009**, *92*, 1153–1177. [CrossRef]
14. Zheng, T.; Wu, J.; Xiao, D.; Zhu, J. Recent development in lead-free perovskite piezoelectric bulk materials. *Prog. Mater. Sci.* **2018**, *98*, 552–624. [CrossRef]
15. Rödel, J.; Webber, K.G.; Dittmer, R.; Jo, W.; Kimura, M.; Damjanovic, D. Transferring lead-free piezoelectric ceramics into application. *J. Eur. Ceram. Soc.* **2015**, *35*, 1659–1681. [CrossRef]
16. Jo, W.; Dittmer, R.; Acosta, M.; Zang, J.; Groh, C.; Sapper, E.; Wang, K.; Rödel, J. Giant electric-field-induced strains in lead-free ceramics for actuator applications—Status and perspective. *J. Electroceramics* **2012**, *29*, 71–93. [CrossRef]
17. Zhang, S.T.; Kounga, A.B.; Aulbach, E.; Ehrenberg, H.; Rödel, J. Giant strain in lead-free piezoceramics $Bi_{0.5}Na_{0.5}TiO_3$–$BaTiO_3$–$K_{0.5}Na_{0.5}NbO_3$ system. *Appl. Phys. Lett.* **2007**, *91*, 112906. [CrossRef]
18. Kounga, A.B.; Zhang, S.-T.; Jo, W.; Granzow, T.; Rödel, J. Morphotropic phase boundary in $(1-x)Bi_{0.5}Na_{0.5}TiO_3$–$xK_{0.5}Na_{0.5}NbO_3$ lead-free piezoceramics. *Appl. Phys. Lett.* **2008**, *92*, 222902. [CrossRef]
19. Li, L.; Hao, J.; Xu, Z.; Li, W.; Chu, R. 0.46% unipolar strain in lead-free BNT-BT system modified with Al and Sb. *Mater. Lett.* **2016**, *184*, 152–156. [CrossRef]
20. Jo, W.; Granzow, T.; Aulbach, E.; Rödel, J.; Damjanovic, D. Origin of the large strain response in $(K_{0.5}Na_{0.5})NbO_3$-modified $(Bi_{0.5}Na_{0.5})TiO_3$–$BaTiO_3$ lead-free piezoceramics. *J. Appl. Phys.* **2009**, *105*, 094102. [CrossRef]
21. Zhu, X.; Chen, K.; Li, W.; Wang, K.; Zhang, L.; Tang, X.; Jian, Z.; Liang, Y.; Zhao, R.; Jiang, Y.; et al. NBT-based lead-free ferroelectrics with an ultra-fast charging and discharging rate for pulse devices. *Mater. Today Commun.* **2025**, *46*, 112643. [CrossRef]
22. Lin, Y.; Li, D.; Zhang, M.; Yang, H. $(Na_{0.5}Bi_{0.5})_{0.7}Sr_{0.3}TiO_3$ modified by $Bi(Mg_{2/3}Nb_{1/3})O_3$ ceramics with high energy-storage properties and an ultrafast discharge rate. *J. Mater. Chem. C* **2020**, *8*, 2258–2264. [CrossRef]
23. Takenaka, T.; Maruyama, K.; Sakata, K. $(Bi_{1/2}Na_{1/2})TiO_3$-$BaTiO_3$ System for Lead-Free Piezoelectric Ceramics. *Jpn. J. Appl. Phys.* **1991**, *30*, 2236–2239. [CrossRef]
24. Yu, H.; Ye, Z.G. Dielectric, ferroelectric, and piezoelectric properties of the lead-free $(1-x)(Na_{0.5}Bi_{0.5})TiO_3$-$xBiAlO_3$ solid solution. *Appl. Phys. Lett.* **2008**, *93*, 112902. [CrossRef]
25. Qiao, Y.; Li, W.; Zhang, Y.; Jing, L.; Yang, X.; Gao, C.; Cao, W.; Fei, W. Ba and Mg co-doping to suppress high-temperature dielectric loss in lead-free $Na_{0.5}Bi_{0.5}TiO_3$-based systems. *J. Eur. Ceram. Soc.* **2020**, *40*, 720–727. [CrossRef]
26. Yang, F.; Wu, P.; Sinclair, D.C. Suppression of electrical conductivity and switching of conduction mechanisms in 'stoichiometric' $(Na_{0.5}Bi_{0.5}TiO_3)_{1-x}(BiAlO_3)_x$ $(0 \leq x \leq 0.08)$ solid solutions. *J. Mater. Chem. C* **2017**, *5*, 7243–7252. [CrossRef]
27. Hribar, U.; Spreitzer, M.; Rojac, T.; König, J. Destabilization of the ferroelectric order in $Na_{0.5}Bi_{0.5}TiO_3$–6 wt% $BaTiO_3$ ceramics through doping. *J. Eur. Ceram. Soc.* **2022**, *42*, 3446–3453. [CrossRef]
28. Habib, M.; Munir, M.; Akram, F.; Lee, S.; Song, T.K.; Turak, A.; Kim, M.H.; Hussain, A. Structural evolution and electromechanical properties of $SrTiO_3$-modified $Bi_{0.5}Na_{0.5}TiO_3$–$BaTiO_3$ ceramics prepared by sol-gel and hydrothermal methods. *Mater. Chem. Phys.* **2021**, *266*, 124529. [CrossRef]
29. Li, Y.; Chen, W.; Zhou, J.; Xu, Q.; Sun, H.; Xu, R. Dielectric and piezoelecrtic properties of lead-free $(Na_{0.5}Bi_{0.5})TiO_3$–$NaNbO_3$ ceramics. *Mater. Sci. Eng. B* **2004**, *112*, 5–9. [CrossRef]
30. Hiruma, Y.; Nagata, H.; Takenaka, T. Phase diagrams and electrical properties of $(Bi_{1/2}Na_{1/2})TiO_3$-based solid solutions. *J. Appl. Phys.* **2008**, *104*, 124106. [CrossRef]
31. Chu, B.J.; Chen, D.R.; Li, G.R.; Yin, Q.R. Electrical properties of $Na_{1/2}Bi_{1/2}$TiO3–$BaTiO_3$ ceramics. *J. Eur. Ceram. Soc.* **2002**, *22*, 2115–2121. [CrossRef]
32. Yang, Z.; Liu, B.; Wei, L.; Hou, Y. Structure and electrical properties of $(1-x)Bi_{0.5}Na_{0.5}TiO_3$–$xBi_{0.5}K_{0.5}TiO_3$ ceramics near morphotropic phase boundary. *Mater. Res. Bull.* **2008**, *43*, 81–89. [CrossRef]
33. Sasaki, A.; Chiba, T.; Mamiya, Y.; Otsuki, E. Dielectric and Piezoelectric Properties of $(Bi_{0.5}Na_{0.5})TiO_3$–$(Bi_{0.5}K_{0.5})TiO_3$ Systems. *Jpn. J. Appl. Phy* **1999**, *38*, 5564. [CrossRef]
34. Hiruma, Y.; Imai, Y.; Watanabe, Y.; Nagata, H.; Takenaka, T. Large electrostrain near the phase transition temperature of $(Bi_{0.5}Na_{0.5})TiO_3$–$SrTiO_3$ ferroelectric ceramics. *Appl. Phys. Lett.* **2008**, *92*, 262904. [CrossRef]
35. Liu, G.; Dong, J.; Zhang, L.; Yan, Y.; Jing, R.; Jin, L. Phase evolution in $(1-x)(Na_{0.5}Bi_{0.5})TiO_3$-$xSrTiO_3$ solid solutions: A study focusing on dielectric and ferroelectric characteristics. *J. Mater.* **2020**, *6*, 677–691. [CrossRef]
36. Shvartsman, V.V.; Lupascu, D.C. Lead-Free Relaxor Ferroelectrics. *J. Am. Ceram. Soc.* **2012**, *95*, 1–26. [CrossRef]
37. Dittmer, R.; Gobeljic, D.; Jo, W.; Shvartsman, V.V.; Lupascu, D.C.; Jones, J.L.; Rödel, J. Ergodicity reflected in macroscopic and microscopic field-dependent behavior of BNT-based relaxors. *J. Appl. Phys.* **2014**, *115*, 084111. [CrossRef]
38. Slabki, M.; Venkataraman, L.K.; Rojac, T.; Rödel, J.; Koruza, J. Thermal stability of the electromechanical properties in acceptor-doped and composite-hardened $(Na_{1/2}Bi_{1/2})TiO_3$–$BaTiO_3$ ferroelectrics. *J. Appl. Phys.* **2021**, *130*, 014101. [CrossRef]
39. Wohninsland, A.; Fetzer, A.K.; Broughton, R.; Jones, J.L.; Lalitha, K.V. Structural and microstructural description of relaxor-ferroelectric transition in quenched $Na_{1/2}Bi_{1/2}TiO_3$-$BaTiO_3$. *J. Mater.* **2022**, *8*, 823–832. [CrossRef]

40. Takenaka, T.; Nagata, H.; Hiruma, Y. Phase Transition Temperatures and Piezoelectric Properties of $(Bi_{1/2}Na_{1/2})TiO_3$-and $(Bi_{1/2}K_{1/2})TiO_3$-Based Bismuth Perovskite Lead-Free Ferroelectric Ceramics. *IEEE Trans. Ultrason. Ferroelectr. Freq. Control* **2009**, *56*, 1595–1612. [CrossRef] [PubMed]
41. Hiruma, Y.; Nagata, H.; Takenaka, T. Phase Transition Temperatures and Piezoelectric Properties of $(Bi_{1/2}Na_{1/2})TiO_3$–$(Bi_{1/2}K_{1/2})TiO_3$–$BaTiO_3$ Lead-Free Piezoelectric Ceramics. *Jpn. J. Appl. Phy* **2006**, *45*, 7409–7412. [CrossRef]
42. Zhu, Z.; Luo, L.; Wang, F.; Du, P.; Zhou, X.; Zhang, Q.; Li, W.; Wang, Y. Improved depolarization temperature via the ordered alignment of defect dipoles in $(Na_{0.5}Bi_{0.5})TiO_3$-$BaTiO_3$ ceramics. *J. Eur. Ceram. Soc.* **2020**, *40*, 689–698. [CrossRef]
43. Guo, Y.; Gu, M.; Luo, H. Antiferroelectric Phase and Pyroelectric Response in $(Na_yBi_z)Ti_{1-x}O_{3(1-x)}$–$x$$BaTiO_3$ Ceramics. *J. Am. Ceram. Soc.* **2011**, *94*, 1350–1353. [CrossRef]
44. Sapper, E.; Novak, N.; Jo, W.; Granzow, T.; Rödel, J. Electric-field–temperature phase diagram of the ferroelectric relaxor system $(1-x)Bi_{1/2}Na_{1/2}TiO_3 - xBaTiO_3$ doped with manganese. *J. Appl. Phys.* **2014**, *115*, 194104. [CrossRef]
45. Yan, B.; Fan, H.; Wang, C.; Zhang, M.; Yadav, A.K.; Zheng, X.; Wang, H.; Du, Z. Giant electro-strain and enhanced energy storage performance of $(Y_{0.5}Ta_{0.5})^{4+}$ co-doped $0.94(Bi_{0.5}Na_{0.5})TiO_3$-$0.06BaTiO_3$ lead-free ceramics. *Ceram. Int.* **2020**, *46*, 281–288. [CrossRef]
46. Teranishi, S.; Suzuki, M.; Noguchi, Y.; Miyayama, M.; Moriyoshi, C.; Kuroiwa, Y.; Tawa, K.; Mori, S. Giant strain in lead-free $(Bi_{0.5}Na_{0.5})TiO_3$-based single crystals. *Appl. Phys. Lett.* **2008**, *92*, 182905. [CrossRef]
47. Krauss, W.; Schütz, D.; Mautner, F.A.; Feteira, A.; Reichmann, K. Piezoelectric properties and phase transition temperatures of the solid solution of $(1-x)(Bi_{0.5}Na_{0.5})TiO_3$–$x$$SrTiO_3$. *J. Eur. Ceram. Soc.* **2010**, *30*, 1827–1832. [CrossRef]
48. Rahman, J.U.; Hussain, A.; Maqbool, A.; Song, T.K.; Kim, W.J.; Kim, S.S.; Kim, M.H. Dielectric, ferroelectric and field-induced strain response of lead-free $BaZrO_3$-modified $Bi_{0.5}Na_{0.5}TiO_3$ ceramics. *Curr. Appl. Phys.* **2014**, *14*, 331–336. [CrossRef]
49. Zhao, H.; Ren, P.; Wang, J.; Wang, Y.; Shen, M.; Liu, L.; Wang, X.; Dong, G.; Zhao, G.; Hua, D. Low hysteresis and temperature stable electrostrain in $0.97(0.94Na_{0.5}Bi_{0.5}TiO_3$-$0.06BaTiO_3)$-$0.03AgNbO_3/x$ZnO composite ceramics. *Ceram. Int.* **2021**, *47*, 25296–25303. [CrossRef]
50. Cao, W.; Sheng, J.; Xu, D.; Li, W. Large strain under low electric field in NBT-KBT-BT ceramics synthesized by Sol–Gel approach. *J. Mater. Sci. Mater. Electron.* **2021**, *32*, 9500–9508. [CrossRef]
51. Lee, H.B.; Heo, D.J.; Malik, R.A.; Yoon, C.H.; Han, H.S.; Lee, J.S. Lead-free $Bi_{1/2}(Na_{0.82}K_{0.18})_{1/2}TiO_3$ ceramics exhibiting large strain with small hysteresis. *Ceram. Int.* **2013**, *39*, S705–S708. [CrossRef]
52. Pham, K.N.; Hussain, A.; Ahn, C.W.; Kim, W.; Jeong, S.J.; Lee, J.S. Giant strain in Nb-doped $Bi_{0.5}(Na_{0.82}K_{0.18})0.5TiO_3$ lead-free electromechanical ceramics. *Mater. Lett.* **2010**, *64*, 2219–2222. [CrossRef]
53. Luo, W.Q.; Shen, Z.Y.; Yu, Y.Y.; Song, F.S.; Wang, Z.M.; Li, Y.M. Structure and dielectric properties of NBT-xBT-ST lead-free ceramics for energy storage. *J. Adv. Dielectr.* **2018**, *8*, 1820004. [CrossRef]
54. Wang, K.; Hussain, A.; Jo, W.; Rödel, J. Temperature-Dependent Properties of $(Bi_{1/2}Na_{1/2})TiO_3$–$(Bi_{1/2}K_{1/2})TiO_3$–$SrTiO_3$ Lead-Free Piezoceramics. *J. Am. Ceram. Soc.* **2012**, *95*, 2241–2247. [CrossRef]
55. Yoo, J.; Oh, D.; Jeong, Y.; Hong, J.; Jung, M. Dielectric and piezoelectric characteristics of lead-free $Bi_{0.5}(Na_{0.84}K_{0.16})_{0.5}TiO_3$ ceramics substituted with Sr. *Mater. Lett.* **2004**, *58*, 3831–3835. [CrossRef]
56. Duong, T.A.; Han, H.S.; Hong, Y.H.; Park, Y.S.; Nguyen, H.T.K.; Dinh, T.H.; Lee, J.S. Dielectric and piezoelectric properties of $Bi_{1/2}Na_{1/2}TiO_3$–$SrTiO_3$ lead–free ceramics. *J. Electroceramics* **2018**, *41*, 73–79. [CrossRef]
57. Kang, Y.; Linh, V.N.; Duong, T.A.; Ahn, C.W.; Kim, B.W.; Lee, J.S.; Han, H.S. The understanding of large electromechanical strain under low electric field in lead-free BNT-based relaxor. *J. Korean Ceram. Soc.* **2025**, *62*, 153–162. [CrossRef]
58. Wang, F.; Xu, M.; Tang, Y.; Wang, T.; Shi, W.; Leung, C.M. Large Strain Response in the Ternary $Bi_{0.5}Na_{0.5}TiO_3$–$BaTiO_3$–$SrTiO_3$ Solid Solutions. *J. Am. Ceram. Soc.* **2012**, *95*, 1955–1959. [CrossRef]
59. Wang, F.; Jin, C.; Yao, Q.; Shi, W. Large electrostrictive effect in ternary $Bi_{0.5}Na_{0.5}TiO_3$-based solid solutions. *J. Appl. Phys.* **2013**, *114*, 027004. [CrossRef]
60. Kang, S.J.L.; Yoon, K.J. Densification of ceramics containing entrapped gases. *J. Eur. Ceram. Soc.* **1989**, *5*, 135–139. [CrossRef]
61. Kang, S.J.L. *Sintering: Densification, Grain Growth & Microstructure*; Elsevier Butterworth-Heinemann: Oxford, UK, 2005; pp. 57–87.
62. German, R.M. Liquid-Phase Sintering. In *Sintering Theory and Practice*; Wiley: New York, NY, USA, 1996; pp. 225–312.
63. Coble, R.L. Sintering Alumina: Effect of Atmospheres. *J. Am. Ceram. Soc.* **1962**, *45*, 123–127. [CrossRef]
64. Kang, S.J.L. What We Should Consider for Full Densification when Sintering. *Materials* **2020**, *13*, 3578. [CrossRef]
65. Choi, J.J.; Ryu, J.; Kim, H.E. Microstructural Evolution of Transparent PLZT Ceramics Sintered in Air and Oxygen Atmospheres. *J. Am. Ceram. Soc.* **2001**, *84*, 1465–1469. [CrossRef]
66. Chen, C.S.; Chen, P.Y.; Tu, C.S.; Chang, T.L.; Chai, C.K. The effects of sintering atmosphere on microstructures and electrical properties of lead-free $(Bi_{0.5}Na_{0.5})TiO_3$-based ceramics. *Ceram. Int.* **2014**, *40*, 9591–9598. [CrossRef]
67. Chen, X.; Pan, W.; Tian, H.; Gong, X.; Bian, X.; Liu, P. Microstructure, dielectric and ferroelectric properties of $0.94Bi_{0.5}Na_{0.5}TiO_3$–$0.06BaTiO_3$ (NBTB) and $0.05BiFeO_3$–0.95NBTB ceramics: Effect of sintering atmosphere. *J. Alloys Compd.* **2011**, *509*, 1824–1829. [CrossRef]

68. Chun, M.P.; Kang, K.M.; Cho, J.H.; Kim, B.I. Effect of the Firing Conditions on the Phase Formation of Alkali Metal Niobate Piezoelectric Ceramics. *J. Korean Phys. Soc.* **2011**, *59*, 2583–2588. [CrossRef]
69. Che, Z.; Ma, L.; Luo, G.; Xu, C.; Cen, Z.; Feng, Q.; Chen, X.; Ren, K.; Luo, N. Phase structure and defect engineering in $(Bi_{0.5}Na_{0.5})TiO_3$-based relaxor antiferroelectrics toward excellent energy storage performance. *Nano Energy* **2022**, *100*, 107484. [CrossRef]
70. Liu, X.; Rao, R.; Shi, J.; He, J.; Zhao, Y.; Liu, J.; Du, H. Effect of oxygen vacancy and A-site-deficiency on the dielectric performance of BNT-BT-BST relaxors. *J. Alloys Compd.* **2021**, *875*, 159999. [CrossRef]
71. Cao, W.; Li, W.; Zhang, T.; Sheng, J.; Hou, Y.; Feng, Y.; Yu, Y.; Fei, W. High-Energy Storage Density and Efficiency of (1−x)[0.94 NBT–0.06 BT]–xST Lead-Free Ceramics. *Energy Technol.* **2015**, *3*, 1198–1204. [CrossRef]
72. Andleeb, K.; Trung, D.T.; Fisher, J.G.; Tran, T.T.H.; Lee, J.S.; Choi, W.J.; Jo, W. Fabrication of Textured $0.685(Na_{0.5}Bi_{0.5})TiO_3$-$0.065BaTiO_3$-$0.25SrTiO_3$ Electrostrictive Ceramics by Templated Grain Growth Using $NaNbO_3$ Templates and Characterization of Their Electrical Properties. *Crystals* **2024**, *14*, 861. [CrossRef]
73. German, R.M. Microstructure and Processing Relations in Solid-State Sintering. In *Sintering Theory and Practice*; Wiley: New York, NY, USA, 1996; pp. 142–177.
74. Moon, K.S.; Kang, S.J.L. Coarsening Behavior of Round-Edged Cubic Grains in the $Na_{1/2}Bi_{1/2}TiO_3$-$BaTiO_3$ System. *J. Am. Ceram. Soc.* **2008**, *91*, 3191–3196. [CrossRef]
75. Le, P.G.; Lee, J.S.; Kim, H.P.; Jo, W.; Xie, H.; Chang, Y.; Ge, W.; Fisher, J.G. Top-seeded solid-state single crystal growth of $0.75(Na_{0.5}Bi_{0.5})TiO_3$-$0.25SrTiO_3$ single crystals in oxygen and their characterization. *J. Korean Ceram. Soc.* **2024**, *61*, 1036–1049. [CrossRef]
76. Zhang, A.; Jing, R.; Zhuang, M.; Hou, H.; Zhang, L.; Zhang, J.; Lu, X.; Yan, Y.; Du, H.; Jin, L. Nonstoichiometric effect of A-site complex ions on structural, dielectric, ferroelectric, and electrostrain properties of bismuth sodium titanate ceramics. *Ceram. Int.* **2021**, *47*, 32747–32755. [CrossRef]
77. Li, M.; Zhang, H.; Cook, S.N.; Li, L.; Kilner, J.A.; Reaney, I.M.; Sinclair, D.C. Dramatic Influence of A-Site Nonstoichiometry on the Electrical Conductivity and Conduction Mechanisms in the Perovskite Oxide $Na_{0.5}Bi_{0.5}TiO_3$. *Chem. Mater.* **2015**, *27*, 629–634. [CrossRef]
78. Yang, F.; Li, M.; Li, L.; Wu, P.; Pradal-Velázquez, E.; Sinclair, D.C. Defect chemistry and electrical properties of sodium bismuth titanate perovskite. *J. Mater. Chem. A* **2018**, *6*, 5243–5254. [CrossRef]
79. Xu, C.; Lin, D.; Kwok, K.W. Structure, electrical properties and depolarization temperature of $(Bi_{0.5}Na_{0.5})TiO_3$–$BaTiO_3$ lead-free piezoelectric ceramics. *Solid State Sci.* **2008**, *10*, 934–940. [CrossRef]
80. Guo, Y.; Liu, Y.; Withers, R.L.; Brink, F.; Chen, H. Large Electric Field-Induced Strain and Antiferroelectric Behavior in $(1-x)(Na_{0.5}Bi_{0.5})TiO_3$-$xBaTiO_3$ Ceramics. *Chem. Mater.* **2011**, *23*, 219–228. [CrossRef]
81. Sakata, K.; Masuda, Y. Ferroelectric and antiferroelectric properties of $(Na_{0.5}Bi_{0.5})TiO_3$-$SrTiO_3$ solid solution ceramics. *Ferroelectrics* **1974**, *7*, 347–349. [CrossRef]
82. Jo, W.; Schaab, S.; Sapper, E.; Schmitt, L.A.; Kleebe, H.J.; Bell, A.J.; Rödel, J. On the phase identity and its thermal evolution of lead free $(Bi_{1/2}Na_{1/2})TiO_3$-6 mol% $BaTiO_3$. *J. Appl. Phys.* **2011**, *110*, 074106. [CrossRef]
83. Schmitt, L.A.; Kling, J.; Hinterstein, M.; Hoelzel, M.; Jo, W.; Kleebe, H.J.; Fuess, H. Structural investigations on lead-free $Bi_{1/2}Na_{1/2}TiO_3$-based piezoceramics. *J. Mater. Sci.* **2011**, *46*, 4368–4376. [CrossRef]
84. Liu, L.; Shi, D.; Knapp, M.; Ehrenberg, H.; Fang, L.; Chen, J. Large strain response based on relaxor-antiferroelectric coherence in $Bi_{0.5}Na_{0.5}TiO_3$–$SrTiO_3$–$(K_{0.5}Na_{0.5})NbO_3$ solid solutions. *J. Appl. Phys.* **2014**, *116*, 184104. [CrossRef]
85. Yao, K.; Zhou, C.; Li, Q.; Xiao, Z.; Yuan, C.; Xu, J.; Chen, G.; Rao, G. Large electrostrictive coefficient with optimized Electro-Strain in BNT-based ceramics with ergodic state. *Mater. Sci. Eng. B* **2022**, *283*, 115828. [CrossRef]
86. Shi, J.; Fan, H.; Liu, X.; Bell, A.J. Large Electrostrictive Strain in $(Bi_{0.5}Na_{0.5})TiO_3$–$BaTiO_3$–$(Sr_{0.7}Bi_{0.2})TiO_3$ Solid Solutions. *J. Am. Ceram. Soc.* **2014**, *97*, 848–853. [CrossRef]
87. Wang, Z.; Zhang, L.; Kang, R.; Mao, P.; Kang, F.; Sun, Q.; Wang, J. High temperature dielectric stable $(1-x)[(Na_{0.5}Bi_{0.5})_{0.92}Ba_{0.08}]_{0.955}La_{0.03}TiO_3$-$xNaNbO_3$ system with ultra-low dielectric loss range through optimizing the defect chemistry. *J. Alloys Compd.* **2020**, *846*, 156308. [CrossRef]
88. Selvamani, R.; Singh, G.; Tiwari, V.S.; Gupta, P.K. Oxygen vacancy related relaxation and conduction behavior in $(1-x)$ NBT-$xBiCrO_3$ solid solution. *Phys. Status Solidi (A)* **2012**, *209*, 118–125. [CrossRef]
89. Bonanos, N.; Steele, B.C.H.; Butler, E.P. Applications of Impedance Spectroscopy: Characterization of Materials. In *Impedance Spectroscopy Theory, Experiment and Applications Second Edition*; Barsoukov, E., Macdonald, J.R., Eds.; Wiley-Interscience: Hoboken, NJ, USA, 2005; pp. 205–263.
90. Suchanicz, J.; Kluczewska-Chmielarz, K.; Sitko, D.; Jagło, G. Electrical transport in lead-free $Na_{0.5}Bi_{0.5}TiO_3$ ceramics. *J. Adv. Ceram.* **2021**, *10*, 152–165. [CrossRef]

91. Zhang, S.T.; Kounga, A.B.; Aulbach, E.; Jo, W.; Granzow, T.; Ehrenberg, H.; Rödel, J. Lead-free piezoceramics with giant strain in the system $Bi_{0.5}Na_{0.5}TiO_3$–$BaTiO_3$–$K_{0.5}Na_{0.5}NbO_3$. II. Temperature dependent properties. *J. Appl. Phys.* **2008**, *103*, 034108. [CrossRef]
92. Ayuningsih, A.; Ecebas, N.; Tran, T.H.T.; Fisher, J.G.; Lee, J.-S.; Choi, W.-J.; Jo, W. Texturing $(Na_{0.5}Bi_{0.5})TiO_3$-$KNbO_3$-$SrTiO_3$ Electrostrictive Ce-ramics by Templated Grain Growth Using $(Na_{0.5}Bi_{0.5})TiO_3$ Platelets. *Inorganics* **2025**, *13*, 387. [CrossRef]
93. Zhou, X.; Yang, H.; Xue, G.; Luo, H.; Zhang, D. Optimized strain performance in <001>-textured $Bi_{0.5}Na_{0.5}TiO_3$-based ceramics with ergodic relaxor state and core—Shell microstructure. *J. Adv. Ceram.* **2022**, *11*, 1542–1558. [CrossRef]
94. Dong, G.; Fan, H.; Liu, L.; Ren, P.; Cheng, Z.; Zhang, S. Large electrostrain in $Bi_{1/2}Na_{1/2}TiO_3$-based relaxor ferroelectrics: A case study of $Bi_{1/2}Na_{1/2}TiO_3$-$Bi_{1/2}K_{1/2}TiO_3$-$Bi(Ni_{2/3}Nb_{1/3})O_3$ ceramics. *J. Mater.* **2021**, *7*, 593–602. [CrossRef]
95. Ehara, Y.; Novak, N.; Ayrikyan, A.; Geiger, P.T.; Webber, K.G. Phase transformation induced by electric field and mechanical stress in Mn-doped $(Bi_{1/2}Na_{1/2})TiO_3$-$(Bi_{1/2}K_{1/2})TiO_3$ ceramics. *J. Appl. Phys.* **2016**, *120*, 174103. [CrossRef]
96. Khan, N.U.; Yun, W.S.; Ullah, A.; Ali, S.; Sheeraz, M.; Ullah, A.; Kim, I.W.; Ahn, C.W. Large electrostrictive response via tailoring ergodic relaxor state in $Bi_{1/2}Na_{1/2}TiO_3$-based ceramics with $Bi(Mn_{1/2}Ce_{1/2})O_3$ end-member. *Ceram. Int.* **2024**, *50*, 8790–8799. [CrossRef]
97. Wang, Z.; Zhao, J.; Zhang, N.; Ren, W.; Zheng, K.; Quan, Y.; Zhuang, J.; Zhang, Y.; Jiang, L.; Wang, L.; et al. Optimizing strain response in lead-free $(Bi_{0.5}Na_{0.5})TiO_3$-$BaTiO_3$-$NaNbO_3$ solid solutions via ferroelectric/(non-)ergodic relaxor phase boundary engineering. *J. Mater.* **2023**, *9*, 244–255. [CrossRef]
98. Fromling, T.; Steiner, S.; Ayrikyan, A.; Bremecker, D.; Durrschnabel, M.; Molina-Luna, L.; Kleebe, H.-J.; Hutter, H.; Webber, K.G.; Acosta, M. Designing properties of $(Na_{1/2}Bi_x)TiO_3$-based materials through A-site non-stoichiometry. *J. Mater. Chem. C* **2018**, *6*, 738–744. [CrossRef]
99. Kang, S.J.L. Grain Growth and Densification in Porous Materials. In *Sintering: Densification, Grain Growth & Microstructure*; Elsevier Butterworth Heineman: Oxford, UK, 2005; pp. 145–170.
100. German, R.M. Solid-State Sintering Fundamentals. In *Sintering Theory and Practice*; Wiley: New York, NY, USA, 1996.
101. Kim, J.J.; Kim, B.K.; Song, B.M.; Kim, D.Y.; Yoon, D.N. Effect of Sintering Atmosphere on Isolated Pores During the Liquid-Phase Sintering of MgO-$CaMgSiO_4$. *J. Am. Ceram. Soc.* **1987**, *70*, 734–737. [CrossRef]
102. Paek, Y.K.; Eun, K.Y.; Kang, S.J.L. Effect of Sintering Atmosphere on Densification of MgO-Doped Al_2O_3. *J. Am. Ceram. Soc.* **1988**, *71*, C-380–C-382. [CrossRef]
103. Du, J.; Huang, X.; Wang, M.; Zhang, H. Densification process of a 95% alumina ceramic during the intermediate stage of sintering in air, and O_2. *Ceram. Int.* **2023**, *49*, 33407–33412. [CrossRef]
104. Hajime, N.; Tadashi, T. Lead-Free Piezoelectric Ceramics of $(Bi_{1/2}Na_{1/2})TiO_3$–$1/2(Bi_2O_3{\cdot}Sc_2O_3)$ System. *Jpn. J. Appl. Phy* **1997**, *36*, 6055. [CrossRef]
105. Wang, X.X.; Tang, X.G.; Kwok, K.W.; Chan, H.L.W.; Choy, C.L. Effect of excess Bi_2O_3 on the electrical properties and microstructure of $(Bi_{1/2}Na_{1/2})TiO_3$ ceramics. *Appl. Phys. A* **2005**, *80*, 1071–1075. [CrossRef]
106. Wang, J.; Yang, L.; He, G.; Hu, Z. Effects of sintering temperature on the energy storage performance of $NaNbO_3$-doped NBT-based dielectric ceramics. *Ceram. Int.* **2025**, *51*, 179–186. [CrossRef]
107. Zhang, Y.R.; Li, J.F.; Zhang, B.P. Enhancing Electrical Properties in NBT–KBT Lead-Free Piezoelectric Ceramics by Optimizing Sintering Temperature. *J. Am. Ceram. Soc.* **2008**, *91*, 2716–2719. [CrossRef]
108. Turki, O.; Slimani, A.; Sassi, Z.; Khemakhem, H.; Abdelmoula, N.; Lebrun, L. Effect of sintering temperature of NBT–6BT lead-free ceramics on the structural, ferroelectric and piezoelectric properties. *Appl. Phys. A* **2022**, *128*, 186. [CrossRef]
109. Fisher, J.G.; Kang, S.J.L. Strategies and practices for suppressing abnormal grain growth during liquid phase sintering. *J. Am. Ceram. Soc.* **2019**, *102*, 717–735. [CrossRef]
110. Jung, Y.I.; Yoon, D.Y.; Kang, S.J.L. Coarsening of polyhedral grains in a liquid matrix. *J. Mater. Res.* **2009**, *24*, 2949–2959. [CrossRef]
111. Kang, S.J.L. *Sintering: Densification, Grain Growth & Microstructure*; Elsevier Butterworth Heinemann: Oxford, UK, 2005; pp. 117–124.
112. Lifshitz, I.M.; Slyozov, V.V. The kinetics of precipitation from supersaturated solid solutions. *J. Phys. Chem. Solids* **1961**, *19*, 35–50. [CrossRef]
113. Wagner, C. Theorie der Alterung von Niederschlägen durch Umlösen (Ostwald-Reifung). *Z. Elektrochem. Ber. Bunsenges. Phys. Chem.* **1961**, *65*, 581–591. [CrossRef]
114. Kang, S.J.L. Grain Shape and Grain Growth in a Liquid Matrix. In *Sintering: Densification, Grain Growth & Microstructure*; Elsevier Butterworth Heinemann: Oxford, UK, 2005; pp. 205–226.
115. Yoon, B.K.; Lee, B.A.; Kang, S.J.L. Growth behavior of rounded (Ti,W)C and faceted WC grains in a Co matrix during liquid phase sintering. *Acta Mater.* **2005**, *53*, 4677–4685. [CrossRef]
116. Kang, S.J.L.; Lee, M.G.; An, S.M. Microstructural Evolution During Sintering with Control of the Interface Structure. *J. Am. Ceram. Soc.* **2009**, *92*, 1464–1471. [CrossRef]

117. Kang, S.J.L.; Ko, S.Y.; Moon, S.Y. Mixed control of boundary migration and the principle of microstructural evolution. *J. Ceram. Soc. Jpn.* **2016**, *124*, 259–267. [CrossRef]
118. Brook, R.J. Pore-Grain Boundary Interactions and Grain Growth. *J. Am. Ceram. Soc.* **1969**, *52*, 56–57. [CrossRef]
119. Gladman, T. The theory and inhibition of abnormal grain growth in steels. *JOM* **1992**, *44*, 21–24. [CrossRef]
120. Kang, S.J.L. Normal Grain Growth and Second-Phase Particles. In *Sintering: Densification, Grain Growth & Microstructure*; Elsevier Butterworth Heinemann: Oxford, UK, 2005; pp. 91–96.
121. Hennings, D.F.K.; Janssen, R.; Reynen, P.J.L. Control of Liquid-Phase-Enhanced Discontinuous Grain Growth in Barium Titanate. *J. Am. Ceram. Soc.* **1987**, *70*, 23–27. [CrossRef]
122. Dillon, S.J.; Tang, M.; Carter, W.C.; Harmer, M.P. Complexion: A new concept for kinetic engineering in materials science. *Acta Mater.* **2007**, *55*, 6208–6218. [CrossRef]
123. Cantwell, P.R.; Tang, M.; Dillon, S.J.; Luo, J.; Rohrer, G.S.; Harmer, M.P. Grain boundary complexions. *Acta Mater.* **2014**, *62*, 1–48. [CrossRef]
124. Kim, S.G.; Park, Y.B. Grain boundary segregation, solute drag and abnormal grain growth. *Acta Mater.* **2008**, *56*, 3739–3753. [CrossRef]
125. Kang, S.J.L.; Park, J.H.; Ko, S.Y.; Lee, H.Y. Solid-State Conversion of Single Crystals: The Principle and the State-of-the-Art. *J. Am. Ceram. Soc.* **2015**, *98*, 347–360. [CrossRef]
126. Hirth, J.P.; Pound, G.M. Growth and Evaporation of Liquids and Dislocation-Free Crystals. In *Condensation and Evaporation: Nucleation and Growth Kinetics*; Pergamon Press: Oxford, UK, 1963; pp. 77–106.
127. Markov, I.V. *Crystal Growth for Beginners: Fundamentals of Nucleation, Crystal Growth and Epitaxy*, 2nd ed.; World Scientific: Singapore, 2003.
128. Burton, W.K.; Cabrera, N.; Frank, F.C. The Growth of Crystals and the Equilibrium Structure of Their Surfaces. *Philos. Trans. R. Soc. A* **1951**, *243*, 299–358. [CrossRef]
129. Kang, S.J.L.; Jung, Y.I.; Jung, S.H.; Fisher, J.G. Interface Structure-Dependent Grain Growth Behavior in Polycrystals. In *Microstructural Design of Advanced Engineering Materials*; Molodov, D.A., Molodov, D.A., Eds.; Wiley-VCH Verlag GmbH & Co. KGaA.: Weinheim, Germany, 2013; pp. 299–322.
130. Jeong, H.C.; Williams, E.D. Steps on surfaces: Experiment and theory. *Surf. Sci. Rep.* **1999**, *34*, 171–294. [CrossRef]
131. Cho, Y.K.; Yoon, D.Y. Surface Roughening Transition and Coarsening of NbC Grains in Liquid Cobalt-Rich Matrix. *J. Am. Ceram. Soc.* **2004**, *87*, 443–448. [CrossRef]
132. Lee, H.R.; Kim, D.J.; Hwang, N.M.; Kim, D.Y. Role of Vanadium Carbide Additive during Sintering of WC–Co: Mechanism of Grain Growth Inhibition. *J. Am. Ceram. Soc.* **2003**, *86*, 152–154. [CrossRef]
133. Heo, Y.H.; Jeon, S.C.; Fisher, J.G.; Choi, S.Y.; Hur, K.H.; Kang, S.J.L. Effect of step free energy on delayed abnormal grain growth in a liquid phase-sintered $BaTiO_3$ model system. *J. Eur. Ceram. Soc.* **2011**, *31*, 755–762. [CrossRef]
134. Choi, K.; Hwang, N.M.; Kim, D.Y. Effect of Grain Shape on Abnormal Grain Growth in Liquid-Phase-Sintered Nb1−xTixC–Co Alloys. *J. Am. Ceram. Soc.* **2002**, *85*, 2313–2318. [CrossRef]
135. Seo, C.E.; Yoon, D.Y.; Wallace, J.S.; Blendell, J.E. Dependence of Grain Shape and Growth on PT Content in PbO-Excess PMN–PT. *J. Am. Ceram. Soc.* **2006**, *89*, 1668–1672. [CrossRef]
136. Rheinheimer, W.; Bäurer, M.; Chien, H.; Rohrer, G.S.; Handwerker, C.A.; Blendell, J.E.; Hoffmann, M.J. The equilibrium crystal shape of strontium titanate and its relationship to the grain boundary plane distribution. *Acta Mater.* **2015**, *82*, 32–40. [CrossRef]
137. Rheinheimer, W.; Altermann, F.J.; Hoffmann, M.J. The equilibrium crystal shape of strontium titanate: Impact of donor doping. *Scr. Mater.* **2017**, *127*, 118–121. [CrossRef]
138. Williams, E.D.; Bartelt, N.C. Thermodynamics of Surface Morphology. *Science* **1991**, *251*, 393–400. [CrossRef]
139. West, A.R. *Solid State Chemistry and Its Applications*; John Wiley & Sons: Hoboken, NJ, USA, 2022.
140. Chiang, Y.M.; Birnie, D.; Kingery, W.D. Chapter 2 Defects in Ceramics. In *Physical Ceramics: Principles for Ceramic Science and Engineering*; John Wiley & Sons: New York, NY, USA, 1997; pp. 101–184.
141. Wortis, M. Equilibrium Crystal Shapes and Interfacial Phase Transitions. In *Chemistry and Physics of Solid Surfaces VII*; Vanselow, R., Howe, R., Eds.; Springer: Berlin/Heidelberg, Germany, 1988; pp. 367–405.
142. An, S.M.; Kang, S.J.L. Boundary structural transition and grain growth behavior in $BaTiO_3$ with Nd_2O_3 doping and oxygen partial pressure change. *Acta Mater.* **2011**, *59*, 1964–1973. [CrossRef]
143. Jung, S.H.; Yoon, D.Y.; Kang, S.J.L. Mechanism of abnormal grain growth in ultrafine-grained nickel. *Acta Mater.* **2013**, *61*, 5685–5693. [CrossRef]
144. Rheinheimer, W.; Bäurer, M.; Handwerker, C.A.; Blendell, J.E.; Hoffmann, M.J. Growth of single crystalline seeds into polycrystalline strontium titanate: Anisotropy of the mobility, intrinsic drag effects and kinetic shape of grain boundaries. *Acta Mater.* **2015**, *95*, 111–123. [CrossRef]
145. Moon, K.S.; Rout, D.; Lee, H.Y.; Kang, S.J.L. Effect of TiO_2 addition on grain shape and grain coarsening behavior in $95Na_{1/2}Bi_{1/2}TiO_3$–$5BaTiO_3$. *J. Eur. Ceram. Soc.* **2011**, *31*, 1915–1920. [CrossRef]

146. Le, P.G.; Jo, G.Y.; Ko, S.Y.; Fisher, J.G. The effect of sintering temperature and time on the growth of single crystals of 0.75 $(Na_{0.5}Bi_{0.5})TiO_3$–0.25 $SrTiO_3$ by solid state crystal growth. *J. Electroceramics* **2018**, *40*, 122–137. [CrossRef]
147. Kang, S.S.; Yoon, D.N. Kinetics of grain coarsening during sintering of Co-Cu and Fe-Cu Alloys with low liquid contents. *Metall. Trans. A* **1982**, *13*, 1405–1411. [CrossRef]
148. Rottman, C.; Wortis, M. Statistical mechanics of equilibrium crystal shapes: Interfacial phase diagrams and phase transitions. *Phys. Rep.* **1984**, *103*, 59–79. [CrossRef]
149. Rottman, C.; Wortis, M. Equilibrium crystal shapes for lattice models with nearest-and next-nearest-neighbor interactions. *Phys. Rev. B* **1984**, *29*, 328–339. [CrossRef]
150. Le, P.G.; Tran, H.T.; Lee, J.S.; Fisher, J.G.; Kim, H.P.; Jo, W.; Moon, W.J. Growth of single crystals in the $(Na_{1/2}Bi_{1/2})TiO_3$–$(Sr_{1-x}Ca_x)TiO_3$ system by solid state crystal growth. *J. Adv. Ceram.* **2021**, *10*, 973–990. [CrossRef]
151. Lay, K.W. Grain Growth in UO_2-Al_2O_3 in the Presence of a Liquid Phase. *J. Am. Ceram. Soc.* **1968**, *51*, 373–376. [CrossRef]
152. Makisumi, K.; Kitanaka, Y.; Noguchi, Y.; Miyayama, M. Enhanced polarization properties of ferroelectric $(Bi_{1/2}Na_{1/2})TiO_3$-$Ba(Mg_{1/3}Nb_{2/3})O_3$ single crystals grown under high-pressure oxygen atmosphere. *J. Ceram. Soc. Jpn.* **2017**, *125*, 463–467. [CrossRef]
153. Noguchi, Y.; Tanabe, I.; Suzuki, M.; Miyayama, M. High-quality single crystal growth of Bi-based perovskite ferroelectrics based on defect chemistry. *J. Ceram. Soc. Jpn.* **2008**, *116*, 994–1001. [CrossRef]
154. Jeon, S.C.; Kim, S.Y.; Moon, K.S. Interface structure dependent step free energy and grain growth behavior of core/shell grains in (Y, Mg)-doped $BaTiO_3$ containing a liquid phase. *J. Eur. Ceram. Soc.* **2022**, *42*, 2804–2812. [CrossRef]
155. Bousquet, M.; Duclère, J.R.; Orhan, E.; Boulle, A.; Bachelet, C.; Champeaux, C. Optical properties of an epitaxial $Na_{0.5}Bi_{0.5}TiO_3$ thin film grown by laser ablation: Experimental approach and density functional theory calculations. *J. Appl. Phys.* **2010**, *107*, 104107. [CrossRef]
156. van Benthem, K.; Elsässer, C.; French, R.H. Bulk electronic structure of $SrTiO_3$: Experiment and theory. *J. Appl. Phys.* **2001**, *90*, 6156–6164. [CrossRef]
157. Panthi, G.; Park, M. Approaches for enhancing the photocatalytic activities of barium titanate: A review. *J. Energy Chem.* **2022**, *73*, 160–188. [CrossRef]
158. Li, M.; Pietrowski, M.J.; De Souza, R.A.; Zhang, H.R.; Reaney, I.M.; Cook, S.N.; Kilner, J.A.; Sinclair, D.C. A family of oxide ion conductors based on the ferroelectric perovskite $Na_{0.5}Bi_{0.5}TiO_3$. *Nat. Mater.* **2014**, *13*, 31–35. [CrossRef]
159. Seo, I.T.; Steiner, S.; Frömling, T. The effect of A site non-stoichiometry on $0.94(Na_yBi_x)TiO_3$-$0.06BaTiO_3$. *J. Eur. Ceram. Soc.* **2017**, *37*, 1429–1436. [CrossRef]
160. Hao, J.; Xu, Z.; Chu, R.; Li, W.; Du, J.; Li, G. Ultrahigh strain response with fatigue-free behavior in $(Bi_{0.5}Na_{0.5})TiO_3$-based lead-free piezoelectric ceramics. *J. Phys. D Appl. Phys.* **2015**, *48*, 472001. [CrossRef]
161. Steiner, S.; Seo, I.T.; Ren, P.; Li, M.; Keeble, D.J.; Frömling, T. The effect of Fe-acceptor doping on the electrical properties of $Na_{1/2}Bi_{1/2}TiO_3$ and 0.94 $(Na_{1/2}Bi_{1/2})TiO_3$–0.06 $BaTiO_3$. *J. Am. Ceram. Soc.* **2019**, *102*, 5295–5304. [CrossRef]
162. Li, M.; Li, L.; Zang, J.; Sinclair, D.C. Donor-doping and reduced leakage current in Nb-doped $Na_{0.5}Bi_{0.5}TiO_3$. *Appl. Phys. Lett.* **2015**, *106*, 102904. [CrossRef]
163. Le, P.G.; Pham, T.L.; Nguyen, D.T.; Lee, J.S.; Fisher, J.G.; Kim, H.P.; Jo, W. Solid state crystal growth of single crystals of $0.75(Na_{1/2}Bi_{1/2})TiO_3$-$0.25SrTiO_3$ and their characteristic electrical properties. *J. Asian Ceram. Soc.* **2021**, *9*, 40–51. [CrossRef]
164. Jagło, G.; Kluczewska-Chmielarz, K.; Suchanicz, J.; Kruk, A.; Kania, A.; Sitko, D.; Nowakowska-Malczyk, M.; Łapiński, M.; Stachowski, G. New insights into structural, optical, electrical and thermoelectric behavior of $Na_{0.5}Bi_{0.5}TiO_3$ single crystals. *Sci. Rep.* **2025**, *15*, 2733. [CrossRef]
165. Walenza-Slabe, J.; Gibbons, B.J. Effect of annealing atmosphere pO_2 on leakage current in $80(Bi_{0.5}Na_{0.5})TiO_3$-$20(Bi_{0.5}K_{0.5})TiO_3$ piezoelectric thin films. *Appl. Phys. Lett.* **2017**, *110*, 162904. [CrossRef]
166. Kling, J.; Tan, X.; Jo, W.; Kleebe, H.J.; Fuess, H.; Rödel, J. In Situ Transmission Electron Microscopy of Electric Field-Triggered Reversible Domain Formation in Bi-Based Lead-Free Piezoceramics. *J. Am. Ceram. Soc.* **2010**, *93*, 2452–2455. [CrossRef]
167. He, L.; Vanderbilt, D. First-principles study of oxygen-vacancy pinning of domain walls in $PbTiO_3$. *Phys. Rev. B* **2003**, *68*, 134103. [CrossRef]
168. Hong, L.; Soh, A.K.; Du, Q.G.; Li, J.Y. Interaction of O vacancies and domain structures in single crystal $BaTiO_3$: Two-dimensional ferroelectric model. *Phys. Rev. B* **2008**, *77*, 094104. [CrossRef]
169. Yamamoto, K.; Suzuki, M.; Noguchi, Y.; Miyayama, M. High-Performance $Bi_{0.5}Na_{0.5}TiO_3$ Single Crystals Grown by High-Oxygen-Pressure Flux Method. *Jpn. J. Appl. Phy* **2008**, *47*, 7623–7629. [CrossRef]

https://doi.org/10.3390/cryst16020143